bioRxiv preprint doi: https://doi.org/10.1101/2022.09.09.507263; this version posted September 10, 2022. The copyright holder for this preprint (which was not certified by peer review) is the author/funder. All rights reserved. No reuse allowed without permission.

X-linked adrenoleukodystrophy patient fibroblast-iPSC-derived astrocytes reveal phenotype-specific metabolic, inflammatory, and microRNA alterations

Running head: X-ALD modeling using patient IPSC-derived astrocytes

Parveen Parasar, DVM, PhD[1]; Navtej Kaur, PhD[1]; Laila M Poisson, PhD[2]; Jaspreet Singh, PhD[1,3,*]

[1]Department of Neurology Research, Henry Ford Health, Detroit, MI, USA

[2]Department of Public Health Sciences, Henry Ford Health Systems, Detroit, MI, USA

[3]Department of Physiology, Michigan State University, East Lansing, MI, USA

* Corresponding author

Dr. Jaspreet Singh, PhD

Department of Neurology Research, Henry Ford Hospital, 2799 W. Grand Blvd, Detroit, MI 48202; Email: jsingh2@hfhs.org; Telephone: 313-916-1112.

bioRxiv preprint doi: https://doi.org/10.1101/2022.09.09.507263; this version posted September 10, 2022. The copyright holder for this preprint (which was not certified by peer review) is the author/funder. All rights reserved. No reuse allowed without permission.

SUMMARY FOR SOCIAL MEDIA

X-adrenoleukodystrophy (X-ALD) is an inherited progressive metabolic disorder caused by pathogenic variants in the ABCD1 gene and thus accumulation of very long chain fatty acids in body fluids and tissues. In the absence of genotype-phenotype correlation, clinical outcomes of X-ALD: cerebral inflammatory adrenoleukodystrophy (cALD) and milder adrenomyeloneuropathy (AMN) cannot be predicted and the mechanism of neuroinflammatory response in cALD phenotype remains unknown. Our study investigated metabolic and genetic profile of patient astrocytes derived from healthy control (CTL), AMN, and cALD skin fibroblast-induced pluripotent stem cells with an objective to develop a direct translatable patient-derived model of X-ALD. We, for the first-time, show that astrocytes of cALD revealed significantly higher phosphorylation of STAT3 which can be due to increased Toll-like receptor expression compared to that of AMN whereas AMN astrocytes showed a higher interleukin-6 signaling, resulting in higher anti-inflammatory activity compared to CTL and cALD. In our first report of miRNA sequencing in X-ALD astrocytes, we observed that miR-9 is associated with disease severity. Patient-iPSC derived astrocytes used in this study provide a cellular model system to study mechanisms underlying disease severity in AMN and cALD, and a platform to identify prospective therapeutic targets and investigate or screen drugs for X-ALD.

bioRxiv preprint doi: https://doi.org/10.1101/2022.09.09.507263; this version posted September 10, 2022. The copyright holder for this preprint (which was not certified by peer review) is the author/funder. All rights reserved. No reuse allowed without permission.

ABSTRACT

Objective: The role of astrocytes largely remains to be explored in X-linked adrenoleukodystrophy (X-ALD). Due to limited study models and inaccessibility to patient-tissue samples, we differentiated astrocytes from patient fibroblast-derived induced pluripotent stem cell (iPSCs) which provided a unique system to investigate molecular and etiopathogenetic mechanisms, identify targets, and develop therapeutic agents for X-ALD.

Methods: We reprogrammed fibroblasts from adrenomyeloneuropathy (AMN) and cerebral adrenoleukodystrophy (cALD) patients carrying ABCD1 with pathogenic variants and a control patient to generate iPSCs. We differentiated iPSCs into astrocytes and performed transmission electron microscopy, gene expression, immunoblotting, enzyme-linked immunosorbent assay, miRNA-Seq, and lipidomics to characterize phenotypic and molecular features of patient-derived astrocytes.

Results: These differentiated astrocytes exhibit diseased phenotypes and replicate biochemical and molecular changes found in patients. We confirmed the deletion of ABCD1 gene-encoded ALD protein and identified ABCD1 variant-driven very long chain fatty acid deposition in AMN and cALD astrocytes. Especially, cALD astrocytes showed increased glycolysis, increased signal transducer and transcription activator (STAT)3 activation, higher miR-9 expression in miRNA-Seq analysis, and reduced expression of anti-inflammatory cytokines such as arginase-1 and mannose receptor C-type-1. Consequently, Toll-like receptor-signaling via myeloid differentiation primary response gene 88 (MyD88) and nuclear factor-kappa B (NF-κB; p52 and p65) induced STAT3 and an altered miR-9 expression is a potential contributor to inflammatory milieu in cALD while interleukin-6 -induced anti-inflammatory cytokine production and increased chemotactic CCL-2 (MCP-1) production in AMN potentially favors microglial recruitment protecting its further progression.

Interpretation: We demonstrate for the first time that patient iPSC-derived astrocytes mimic and recapitulate neuroinflammatory and biochemical defects of X-ALD and provide an *in vitro* cellular system to study X-ALD.

bioRxiv preprint doi: https://doi.org/10.1101/2022.09.09.507263; this version posted September 10, 2022. The copyright holder for this preprint (which was not certified by peer review) is the author/funder. All rights reserved. No reuse allowed without permission.

INTRODUCTION

X-linked adrenoleukodystrophy (X-ALD) is a progressive peroxisomal disease due to a defective ABCD1 gene encoding the peroxisomal ABC half-transporter adrenoleukodystrophy (ALD) protein. Deleterious and/or pathogenic variants of ABCD1 impair β-oxidation of fatty acids leading to accumulation of very long chain fatty acids (VLCFAs), predominantly C26:0 in blood and tissues, adversely affecting the brain, spinal cord, and adrenals.[1] More than 650 deleterious variants of ABCD1 have been reported in X-ALD; however, no genotype/clinical phenotype correlation exists.[2]

Phenotypes of X-ALD include rapidly progressive inflammatory demyelinating cerebral adrenoleukodystrophy (cALD), milder adult-onset form, adrenomyeloneuropathy (AMN), and adrenal insufficiency without neurologic involvement. Approximately 35% of affected males develop cALD earlier than 12 years of age. Most cALD patients die within a decade after diagnosis if there is not early intervention. AMN is a gradually developing phenotype, first affecting males with dysfunctional ABCD1 aged 20-30 years. AMN may exist as the pure non-inflammatory axonopathy AMN form, manifesting with gait disturbances and bladder dysfunctions, or as the AMN-cerebral form manifesting with cerebral inflammation in addition to the AMN form. About 30% of AMN patients develop cerebral inflammation, ultimately progressing to the fatal cALD form in adulthood.[1, 2]

Human astrocytes are the major cell population in the central nervous system and play a substantial role in X-ALD pathogenesis. Peroxisomal ABCD1 protein plays a role in mouse astrocyte inflammatory response.[3] We earlier documented that adenosine monophosphate-activated protein kinase α1 (AMPKα1)-loss in cALD patients was associated with higher inflammatory profile in cALD patient-derived cells[4-6]; however, the underlying definitive mechanisms of phenotypic variability and differential inflammatory responses between AMN and cALD phenotypes remain unknown.

Current mouse models[7, 8] poorly represent clinical phenotypic heterogeneity in X-ALD and do not develop neurologic phenotype representative of human cALD phenotype. This begs a clear need for a direct translatable cellular model to study disease mechanisms. In the context of limited models and inaccessibility of human astrocytes, the use of patient induced pluripotent stem cells (iPSCs) are an

bioRxiv preprint doi: https://doi.org/10.1101/2022.09.09.507263; this version posted September 10, 2022. The copyright holder for this preprint (which was not certified by peer review) is the author/funder. All rights reserved. No reuse allowed without permission.

emerging paradigm to study etiopathogenetic mechanisms *in vitro* at the cellular level, screen potential therapeutics, and provide defined conditions to perform research reproducibly.[9] Furthermore, iPSCs retain pluripotency potential to differentiate into any body cell type and carry genetic background of patients and disease-causing genetic variants and defects.[10]

Patient-iPSCs-derived astrocytes enable us to study and uncover molecular mechanisms responsible for transition from milder AMN to severe cALD form and to strategize novel therapeutic targets. Here we demonstrate that reprogrammed iPSCs from normal healthy control (CTL), AMN, and cALD fibroblasts can be differentiated into astrocytes and used as a cellular model to study molecular mechanisms of cALD and AMN. We for the first-time document novel insights into the characterization of X-ALD patient iPSC-derived astrocytes and identify differences between cALD and AMN phenotypes underlying genetic and biochemical perturbations in cALD versus AMN astrocytes and in AMN versus CTL astrocytes.

METHODS

Ethics Approval

The project was approved by Henry Ford Health Institutional Review Board (#13352). The fibroblast samples were previously de-identified specimens and did not involve human subjects.

Derivation of iPSCs and Differentiation into Astrocytes

Human skin fibroblasts were obtained from the National Institute for General Medical Sciences human genetic cell repository at Coriell Institute for Medical Research, Camden, NJ. The samples included normal healthy individual CTL fibroblasts (GM03377; CTL 19 years of age at sampling), AMN fibroblasts (GM07530; AMN 26 years of age at sampling), and cALD (GM04933; cALD 8 years of age at sampling). Skin fibroblasts were generated into iPSCs using the Cytotune2.0 Sendai Virus Reprogramming Kit (Axol Biosciences Ltd). Generated iPSCs were differentiated into astrocytes at Axol Biosciences. CTL, AMN, and ALD astrocytes were characterized using immunofluorescence with astrocyte specific markers. The cells (P5), upon arrival, were frozen in vapor phase nitrogen until used.

iPSC-Derived Astrocyte Culture

bioRxiv preprint doi: https://doi.org/10.1101/2022.09.09.507263; this version posted September 10, 2022. The copyright holder for this preprint (which was not certified by peer review) is the author/funder. All rights reserved. No reuse allowed without permission.

Cells were cultured in astrocyte medium (Neurobasal-A medium, Thermo Fisher Scientific) containing N-21 max (1X, R&D Systems), fetal bovine serum One Shot (1X, Thermo Fisher Scientific), Glutamax (1X, Gibco, Thermo Fisher Scientific), heregulin-β1 (10 ng/mL, Peprotech, Inc.), basic fibroblast growth factor (8 ng/mL, R&D Systems), penicillin-streptomycin (1X, Thermo Fisher Scientific). Cells were seeded at a density of 5 x 10^4 cells/cm^2 (day 0) at 37°C, 5% CO_2 in a humidified incubator. Media was changed every 2 days thereafter.

For cytokine gene expression analysis, the cells were cultured in Neurobasal-A medium without serum) on Matrigel-coated culture plates.

Karyotype Analyses

Human G-banding karyotype analysis was performed using the standard protocol at the Henry Ford Cytogenetics Laboratory. Briefly, cells were metaphase-arrested using KaryoMax (Colcemid, Thermo Fisher Scientific) and fixed using a hypotonic (0.8% sodium citrate) and fixative (3:1 methanol:acetic acid) solution. Cells were equilibrated in Thermotron (Thermotron, Inc.) and dried followed by G-banding with Leishman staining. Four metaphases were analyzed per cell type to identify G-banding. Cells were analyzed as per the Clinical Cytogenetics Standards and Guidelines.[11]

RNA Purification, Complementary DNA Synthesis, and Quantitative Real-Time Polymerase Chain Reaction Gene Expression

Total RNA was extracted using miRNeasy kit (Qiagen) per the manufacturer's protocol. Single-stranded complementary DNA (cDNA) synthesis and real-time polymerase chain reaction (RT-PCR) was conducted using Bio-Rad's CFX96 Real-Time PCR Detection System as previously described.[3, 5] The primer sets were synthesized from Integrated DNA Technologies (Table 1). IQ SYBR Green Supermix was purchased from Bio-Rad. The gene expression was normalized to 60S ribosomal L27 gene. For each gene, cDNA samples were run in triplicates (n = 3).

VLCFA Analysis

CTL, AMN, and cALD astrocytes (2.5 x 10^5 cells) were submitted to Wayne State University Lipidomics Core facility. Saturated (hexacosanoic [C26:0], tetracosanoic [C24:0]), and monounsaturated fatty acids

bioRxiv preprint doi: https://doi.org/10.1101/2022.09.09.507263; this version posted September 10, 2022. The copyright holder for this preprint (which was not certified by peer review) is the author/funder. All rights reserved. No reuse allowed without permission.

[C26:1], and nervonic fatty acids [C24:1]), were calculated as ratios against docosanoic (C22:0) fatty acid as internal control. Lipids were subject to alkaline methanolysis and resulting fatty acid methyl esters were analyzed by gas chromatography-mass spectrophotometry (QP2010 GC-MS system, Shimadzu Scientific Instruments) equipped with Restek column as published earlier.[5]

Mitochondrial Oxygen Consumption and Glycolytic Function Measurement

Oxygen consumption rate (OCR) and extracellular acidification rate (ECAR) were measured in CTL, AMN, and cALD iPSC-derived astrocytes using a Seahorse Bioscience XFe96 Extracellular Flux Analyzer. After 24 hours of culture in 100 mm Matrigel-coated plates (Corning Incorporated), OCR and ECAR were measured as published earlier.[4]

Western Blot Analysis

Cells were homogenized in radioimmunoprecipitation assay/RIPA buffer with Halt protease inhibitor cocktail (Thermo Fisher Scientific). The protein concentration of samples was measured on Qubit 4.0 fluorometer (Thermo Fisher Scientific) and 50-100 µg of total protein was electrophoresed as described earlier.[5, 6] Antibodies used are listed in Table 1.

Transmission Electron Microscopy

One million cells were fixed in 2.5% glutaraldehyde overnight and stained using published protocol[12] with slight modifications. Cells were kept in Eppendorf tubes all the time and re-pelleted if needed before infiltration (with 1:1 mixture of propylene oxide and Araldite resin) step. Cells were kept in infiltration mixture and were not mixed on rocker. Samples were embedded in the mold with the resin and cured overnight at 60°C.

Embedded samples were sectioned120 nm using a EM U67 Ultratome (Leica Microsystems, Inc.) and collected onto 20 mesh copper grids. Dry grids were stained with uranyl acetate and lead citrate with rinses in between. Images were acquired using a Flash transmission electron microscopy equipped with BioSprint camera (Joel USA, Inc.) and image capture software (AMT Imaging Systems).

Reactive Oxygen Species Production

bioRxiv preprint doi: https://doi.org/10.1101/2022.09.09.507263; this version posted September 10, 2022. The copyright holder for this preprint (which was not certified by peer review) is the author/funder. All rights reserved. No reuse allowed without permission.

We used reactive oxygen species (ROS) assay kit (Abcam, Inc.). Cells (1 x 10^5) were plated in triplicate in a 96-well plate and switched to serum free media the next day. Tert-Butyl hydroperoxide 50 µM was added to positive control wells 4 hours before reading the plate. Finally, 2',7'-dichlorofluorescin diacetate 20 µM was added to the wells except unlabeled blank wells. The absorbance was measured at excitation/emission of 485/535 nm.

Nicotinamide Adenine Dinucleotide Assay

Intracellular nicotinamide adenine dinucleotide/nicotinamide adenine dinucleotide hydrogen (NAD/NADH) assay was performed according to the manufacturer's protocol (Cayman Chemical). Briefly, CTL, AMN, and cALD astrocytes were seeded in 96-well plates (1.0 x 10^5 cells/well) and incubated overnight at 37°C and 5% CO_2. Absorbance was measured at 450 nm. NAD/NADH ratio was measured using a NAD^+ standard curve obtained from absorbance of wells containing NAD standards. Assay buffer served as blank.

Mitochondrial DNA Content

Genomic DNA was isolated using DNeasy Blood & Tissue Kit (Qiagen). The mitochondrial DNA (mtDNA) content was calculated using quantitative RT-PCR by measuring the threshold cycle ratio (ΔCt) of a mitochondria-encoded gene mtDNA tRNA Leu (UUR) gene and a nuclear gene β2-microglobulin (Table 1).[13] Data was expressed as mtDNA/nuclear DNA (n = 3).

Enzyme-Linked Immunosorbent Assay

Astrocyte serum-free basal culture supernatants were collected after 72 hours of culture and centrifuged to remove residual cells and stored in -80°C until use. Using enzyme-linked immunosorbent assay Max Deluxe Set (BioLegend) for interleukin (IL)-6, monocyte chemoattractant protein-1 (MCP-1) or C-C motif chemokine ligand 2 (CCL-2), IL-1β, tumor necrosis factor (TNF)-α, IL-12p70, and IL-12/IL-23(p40) following manufacturer's instructions. Standards with known amounts of cytokines were used to determine absolute concentrations of cytokines.

Assay for Nitric Oxide Synthesis

bioRxiv preprint doi: https://doi.org/10.1101/2022.09.09.507263; this version posted September 10, 2022. The copyright holder for this preprint (which was not certified by peer review) is the author/funder. All rights reserved. No reuse allowed without permission.

Production of nitric oxide was determined in cell lysates per the manufacturer's (Sigma Aldrich) instructions. Lysate (100 µl) was added in triplicates along with standards and controls. Griess reagent I and II were added and incubated for 10 minutes at room temperature. Optical density was measured at 540 nm. Assay buffer served as blank for the experiment. Nitrite concentrations were calculated from a standard curve obtained from reaction of nitrogen oxide and Griess reagent II in the assay.

Human Phospho-Kinase Proteome Profiler

We utilized human proteome profiler array to simultaneously detect relative levels of phosphorylation of 37 kinase phosphorylation sites and 2 related total proteins in patient astrocytes. We used 250 µg of cell lysates for each of the parts A and B of the array and followed manufacturers' instructions (R&D Systems).

Data Analysis

The data were analyzed using GraphPad Prism software (version 7.0). Groups were first tested for normality using Kolmogorov-Smirnov. Two-tailed unpaired Student's t-test was used to compare groups with normal distribution or non-parametric Mann-Whitney test with non-normal distribution. Statistical significance was designated for *P*-value of less than 0.05.

Small RNA Library Construction and Sequencing

Small RNA sequencing and informatics was performed by Psomagen, Inc using the QIAseq miRNA Library Kit for Illumina (n = 5). Quality assessment (FastQC v0.11.7), adaptor trimming (Cutadapt 2.8),[14] and rRNA filtering were performed. Mature miRNA sequences and read clusters were aligned to the precursor miRNA sequences of miRBase v22.1 (Bowtie 1.1.2).[15] Read counts were generated using the miRDeep2 Quantifier module and novel miRNA were predicted using the miRDeep2 RNAfold algorithm (miRDeep2 2.0.0.8).[16] The difference in abundance between any two diagnosis groups was estimated by mean fold change and assessed by a negative-binomial Wald-test (R package DEseq2).[17] False discovery was controlled within a two-group comparison with Benjamini-Hochberg corrected *P*-values, with adjusted-p < 0.05 and mean fold change >2 as the threshold for statistical significance. Boxplots were drawn of the miRNA abundance (log10) within the three groups, for the set of commonly altered miRNA.

bioRxiv preprint doi: https://doi.org/10.1101/2022.09.09.507263; this version posted September 10, 2022. The copyright holder for this preprint (which was not certified by peer review) is the author/funder. All rights reserved. No reuse allowed without permission.

Partial least squared discriminant analysis was conducted on this subset for a visualization of the separation between diagnosis groups (R package mixOmics).[18] The first two components were presented in a scatter plot, with 95% confidence region ellipses plotted for each of the three diagnoses. The common set of altered miRNA was also analyzed with the use of QIAGEN Ingenuity Pathway Analysis (IPA; https://digitalinsights.qiagen.com/IPA). Networks of interrelated miRNA and associated molecular components were generated and colored according to observed and predicted levels through the use of QIAGEN IPA.

RESULTS

Characterization of Fibroblasts, iPSCs and Astrocytes

All fibroblasts were characterized and confirmed by nucleoside phosphorylase, glucose-6-phosphate dehydrogenase, and lactate dehydrogenase isoenzyme electrophoresis at National Institute for General Medical Sciences.

iPSCs were successfully reprogrammed from CTL, AMN, and cALD fibroblasts and differentiated into astrocytes. iPSCs stained positive for pluripotency markers OCT4, Sox2, Nanog, and TRA-1-60 pluripotency markers (Fig 1A) and astrocytes confirmed positive for glial fibrillary acidic protein (GFAP), Nestin, aquaporin 4 (AQP4), tubulin βIII, S100-β, aldehyde dehydrogenase 1 (ALDH1), excitatory amino acid transporter 1 (EAAT1), and A2B5 markers with immunofluorescence (Fig 1B). GFAP, S100-β, EAAT1, AQP4, and ALDH1 expression were confirmed by immunoblot analysis and GFAP, S100-β, AQP4, ALDH1, and Nestin was confirmed by quantitative RT-PCR (Fig 1C and D). S100-β protein showed much lower expression in cALD and no expression in AMN astrocytes. AMN and cALD astrocytes showed higher AQP4 expression, suggesting activation of astrocytes.

Karyotype Analyses

The CTL, AMN, and cALD astrocytes displayed apparently normal male karyotyping and G-banding pattern with no evidence of structural or numerical changes. This suggests that reprogramming and differentiation did not alter or induce chromosomal abnormalities in AMN and cALD astrocytes compared

bioRxiv preprint doi: https://doi.org/10.1101/2022.09.09.507263; this version posted September 10, 2022. The copyright holder for this preprint (which was not certified by peer review) is the author/funder. All rights reserved. No reuse allowed without permission.

to CTL astrocytes (Fig 1E-G). Astrocytes were characterized for copy number change (molecular karyotype) using chromosome microarray and no anomaly was detected between CTL, AMN, and cALD astrocytes (data not shown).

AMN and cALD Astrocytes Show Loss of ABCD1 Protein

We confirmed loss of ABCD1 protein in AMN and cALD astrocytes compared to CTL astrocytes by immunoblotting confirming that the ABCD1 gene harbors deleterious variants, and astrocytes derived from affected patients carry those affected ABCD1 genes. On the contrary, ABCD2 protein showed compensatory marked increase in expression in AMN and cALD astrocytes. ABCD3 protein expressed at lower levels and remained unchanged in CTL, AMN, and cALD astrocytes (Fig 2A).

AMN and cALD Astrocytes Accumulated Higher VLCFAs

The hallmark of X-ALD, accumulation of VLCFAs, was confirmed with VLCFA analyses. AMN astrocytes displayed significantly higher levels of saturated (C24:0, C26:0) and monounsaturated (C24:1, C26:1) VLCFA compared to CTL, indicating impaired β-oxidation of VLCFA in AMN astrocytes (Fig 2B). Saturated and monounsaturated VLCFA levels were significantly increased in cALD astrocytes compared to AMN (Fig. 2B)

ELOVL1 catalyzes synthesis of saturated and monounsaturated VLCFAs. We detected four times greater expression of the ELOVL1 gene in cALD over AMN astrocytes ($p < 0.01$) and CTL astrocytes ($p < 0.01$). However, AMN astrocytes did not show significant difference than CTL astrocytes. ELOVL3 gene, on the other hand, did not present a significant difference among healthy and X-ALD astrocytes (Fig 2C).

cALD Astrocytes Show Increased Basal Respiration and Elevated ATP-Linked OCR

VLCFA accumulation causes metabolic alterations in X-ALD[4, 5] and to assess and explore the metabolic profile of AMN and cALD-astrocytes, we performed metabolic flux assay using Seahorse flux analyzer (XFe96). In Cell Mito Stress Test, oligomycin injection inhibits mitochondrial ATP synthase (Complex V), carbonyl cyanide-4 (trifluoromethoxy) phenylhydrazone uncoupler maximizes electron transport chain, and rotenone and antimycin-A inhibit complex I and III (inhibition of electron transport chain). In our Cell Mito Stress Test (Fig 3A), we observed that basal OCR, non-mitochondrial OCR (Fig 3B), ATP linked

bioRxiv preprint doi: https://doi.org/10.1101/2022.09.09.507263; this version posted September 10, 2022. The copyright holder for this preprint (which was not certified by peer review) is the author/funder. All rights reserved. No reuse allowed without permission.

OCR (Fig 3C), maximal respiration, and spare capacity (Fig 3D) were higher in cALD astrocytes compared to AMN astrocytes, indicating that cALD astrocytes possess higher uncoupling, and higher energy needs compared to CTL. ATP assay documented that both AMN and cALD astrocytes have significantly lower ATP production compared to CTL. However, cALD astrocytes produced significantly higher ATP than AMN ($p < 0.05$; Fig 3E).

Intriguingly, we also noticed elevated ECAR in cALD astrocytes (Fig 3F), suggesting enhanced glycolytic mechanisms. Glycolytic stress test to measure ECAR upon injections of glucose, oligomycin, and 2-deoxy-d-glucose documented increased non-glycolytic ECAR and glycolysis in cALD astrocytes compared to that of AMN ($p < 0.001$) and CTL (Fig 3G) and significantly increased glycolytic capacity and glycolytic reserve in cALD astrocytes (Fig 3H and 3I) compared to both AMN ($p < 0.05$) and CTL astrocytes, thus suggesting that cALD astrocytes have increased uncoupling. Astrocytes in cALD are activated due to proinflammatory response and thus show high energetic demands and not only that these cells respond to this metabolic pressure well but also that they are metabolically plastic to meet higher energy demands. cALD astrocytes had significantly decreased glycolytic ATP production rate relative to AMN ($p< 0.05$); however, both AMN and cALD astrocytes observed a significant decrease in glycolytic ATP production rate compared to CTL ($p < 0.05$) (Fig 3J).

Electron Microscopy Reveals Mitochondrial Structure Differences

To explain metabolic differences, we performed electron microscopy on CTL, AMN and cALD astrocytes and analyzed the cellular and mitochondrial structure. Importantly, astrocytes of AMN and cALD contained deposits of lipids (fatty acid droplets) (Fig 4A2 and 4A3) compared to that in CTL astrocytes (Fig 4A1). We also observed, in cALD patient-astrocytes, disrupted cristae structure (Fig 4A6 and 4A9) compared to that in CTL (Fig 4A4 and 4A7) and AMN astrocytes (Fig 4A5 and 4A8). We observed a significantly increased dynamin related protein-1 (DRP-1), a key mitochondrial fission regulator, in both AMN and cALD astrocytes indicative of mitochondrial fragmentation (Fig 4B and C). These salient findings suggest that cALD astrocytes have altered mitochondrial structure and are highly active

bioRxiv preprint doi: https://doi.org/10.1101/2022.09.09.507263; this version posted September 10, 2022. The copyright holder for this preprint (which was not certified by peer review) is the author/funder. All rights reserved. No reuse allowed without permission.

metabolically as shown by higher OCR and potentially upregulate mitochondrial biogenesis to meet the energetic needs of the cells in X-ALD.

Mitochondrial Function and Glycolytic Genes are altered in X-ALD Phenotypes

To assess if the altered OCR and ECAR observed in AMN and cALD astrocytes is a result of changes in gene expression of oxidative phosphorylation (OXPHOS) and glycolytic pathway, we carried out RT-PCR analysis. RT-PCR expression analysis showed several genes related to mitochondrial functions and glycolysis altered in cALD astrocytes. Succinate dehydrogenase complex subunit B (SDHB) and ubiquinol-cytochrome C reductase complex ubiquinone-binding protein QP-C (UQCRQ) showed lower expression in AMN and cALD ($p < 0.05$ and $p < 0.05$, respectively; Fig 4D) astrocytes suggesting that these astrocytes potentially have defective transfer of electrons derived from NADH and succinate, and thus the electrochemical gradient on the inner membrane may be compromised. cALD astrocytes showed significantly higher expression of NDUFA6 (NADH:Ubiquinone Oxidoreductase Subunit A6), citrate synthase, nuclear respiratory factor 1 (all $p < 0.01$; Fig 4D), ATP5B, and peroxisome proliferator-activated receptor gamma coactivator 1-α (PGC1α) compared to AMN astrocytes (both $p < 0.001$; Fig 4D). Similarly, AMN astrocytes showed higher expression of citrate synthase ($p < 0.05$) compared to that of CTL astrocytes (Fig 4D). We performed immunoblotting to detect oxidative phosphorylation subunits in these cells and oxidative phosphorylation. Immunoblot showed decrease in SDHB (Complex II-SDHB) and mitochondrially encoded cytochrome C oxidase I (Complex IV-MTCO1) in cALD astrocytes compared to AMN astrocytes while AMN astrocytes showed increased SDHB and MTCO1 than CTL (Fig 4E).

cALD astrocytes also showed increased expression of Glut-1/SLC2A, HK-I AND -II, GPI, ALDOC, GAPDH, ENO-1, AND PKM2 compared to AMN astrocytes and CTL astrocytes whereas LDHA was not significantly different among the three groups. AMN astrocytes did not show significant difference in these gene expression relative to CTL astrocytes except for PKM2 and GLUT1 (Fig 4F and G).

cALD Astrocytes Produce Higher ROS

bioRxiv preprint doi: https://doi.org/10.1101/2022.09.09.507263; this version posted September 10, 2022. The copyright holder for this preprint (which was not certified by peer review) is the author/funder. All rights reserved. No reuse allowed without permission.

To check whether accumulated VLCFAs induce astrocytes to produce ROS, we performed ROS analysis. cALD and AMN astrocytes showed slightly higher ROS production compared to unlabeled and labeled CTL astrocytes, though the difference did not reach statistical significance. Upon treatment with positive control tert-Butyl hydroperoxide, which produces positive ROS and acts as positive control, there was no increase in ROS in AMN and cALD astrocytes under basal conditions compared to CTL (Fig 4H). However, NADPH oxidase isoforms (NOX) isoforms which have primary role to generate ROS, were upregulated in cALD astrocytes (Fig 4I).

AMN and cALD Astrocytes Show Reduced mtDNA Content

To determine mitochondrial mass or content within X-ALD astrocytes, we measured the mtDNA/nDNA ratio by quantitative RT-PCR. We observed a decreased mtDNA/nuclear DNA ratio in AMN and cALD astrocytes using RT-PCR analysis further suggesting decreased mitochondrial content in X-ALD ($p < 0.05$) (Fig 4J).

Intracellular NAD/NADH Levels are Increased in AMN and cALD Astrocytes

NAD is a cofactor involved in electron transfer functions in redox reactions and regulates glycolysis, tricarboxylic acid cycle, and oxidative phosphorylation. We measured basal NAD/NADH ratio in cultured astrocytes. cALD astrocytes showed significantly higher level of NAD/NADH ratio ($p < 0.001$) compared to AMN astrocytes, which in turn had significantly higher NAD/NADH ratio compared to CTL astrocytes (Fig 4K).

cALD Astrocytes Display Increased IL-1β, Interferon-γ, Nitric Oxide Synthase-2, and IL-23a and Reduced Arginase-1, IL-4, and Mannose Receptor C-Type-1

We and others have previously documented increased proinflammatory gene expression in cALD patient postmortem brain tissue.[5, 19] VLCFA accumulation, is also associated with inflammatory response in ABCD1-silenced mouse astrocytes.[3] We analyzed the inflammatory gene expression in unstimulated AMN and cALD astrocytes. Astrocytes from cALD patients showed upregulated interferon-γ ($p < 0.01$), nitric oxide synthase 2, TNF-α (both $p < 0.05$), IL-17A, and IL-22 (both $p < 0.01$) in comparison to AMN astrocytes (Fig. 5A). IL-12α ($p < 0.01$) and IL-12β ($p < 0.05$) were down-regulated in cALD astrocytes

bioRxiv preprint doi: https://doi.org/10.1101/2022.09.09.507263; this version posted September 10, 2022. The copyright holder for this preprint (which was not certified by peer review) is the author/funder. All rights reserved. No reuse allowed without permission.

compared to AMN and control astrocytes (Fig. 5A). Notably, AMN astrocytes expressed higher expression of IL-6 ($p < 0.01$) and Oncostatin M ($p < 0.05$) compared to healthy control and cALD astrocytes (Fig. 5A). IL-1β ($p < 0.05$) and IL-RA ($p < 0.01$) showed lower expression in both AMN and cALD astrocytes (Fig. 5A). Although, IL-1R showed higher expression in AMN and cALD compared to CTL astrocytes, it did not change between AMN and cALD astrocytes. Similarly, IL-23α expression was comparable among AMN and cALD astrocytes (Fig. 5A). On the other hand, anti-inflammatory cytokines, arginase-1, and mannose receptor C-type-1, were down-regulated (both $p < 0.05$) in cALD compared to AMN astrocytes. IL-4 expression was decreased both in AMN and cALD astrocytes. Fizz-1 did not change significantly between CTL and AMN but was increased in cALD astrocytes (Fig. 5B). IL-10 was significantly decreased in AMN compared to CTL astrocytes and was significantly higher in cALD astrocytes compared to AMN (Fig. 5B)

Owing to the role of CCL-2, a pivotal chemoattractant protein for monocytes, and the other chemokines in pathogenesis of neurological disorders including X-ALD,[19, 20] we analyzed chemokine expressions in unstimulated CTL, AMN, and cALD astrocytes. CCL-2, CCL-3, CCL-4 (all $p < 0.01$), CCL-22 ($p < 0.05$), and CCL-5 ($p < 0.001$), were significantly upregulated in AMN compared to CTL astrocytes (Fig 5C). CCL-2 ($p < 0.01$) and CCL-3 ($p < 0.05$) were significantly downregulated whereas CCL-22 was significantly higher in cALD compared to AMN astrocytes ($p < 0.05$) (Fig 5C). AMN astrocytes expressed significantly higher levels ($p < 0.05$) of chemokine (CC) receptors CCR-1, CCR-2, CCR-3, CCR-5, and CCR-8 compared to CTL astrocytes (Fig 5D). The expression of CCR-1, CCR-3, CCR-5, and CCR-8 receptors was further significantly increased ($p < 0.05$) in cALD astrocytes compared to AMN astrocytes (Fig. 5D). CXCL-1, CXCL-2, and CXCL-8 were significantly upregulated ($p < 0.05$) in AMN astrocytes compared to CTL and were downregulated in cALD astrocytes compared to AMN (Fig. 5E). AMN and CTL astrocytes expressed comparable levels of CXCL10 while cALD astrocytes expressed significantly lower level of CXCL10 against AMN astrocytes and CTL ($p < 0.05$). Both AMN and cALD astrocytes had significantly lower level ($p < 0.05$) of CXCL12 compared to that of CTL (Fig 5E). To further assess alterations in neurotrophic factors, we analyzed mRNA expression of neurotrophic factors (BDNF, CNTF,

bioRxiv preprint doi: https://doi.org/10.1101/2022.09.09.507263; this version posted September 10, 2022. The copyright holder for this preprint (which was not certified by peer review) is the author/funder. All rights reserved. No reuse allowed without permission.

GDNF, NGF, NTF3, and NTF4/5). BDNF was lower in AMN compared to CTL and was further significantly decreased ($p < 0.05$) in cALD compared to AMN (Fig. 5F). CNTF expression was higher ($p < 0.01$) in cALD compared to AMN and CTL astrocytes. There was no significant change in GDNF levels between the three phenotype astrocytes. Both AMN and cALD astrocytes expressed lower NGF ($p < 0.05$) and higher level of NTF3 and NTF4/5 ($p < 0.05$) compared to CTL astrocytes (Fig 5F).

Enzyme-Linked Immunosorbent and Nitrite Assay

AMN astrocytes showed significantly higher ($p < 0.05$) IL-12p40 compared to that in CTL and cALD (Fig 5G). The levels of IL-12p40 were not significantly different in CTL and cALD astrocytes. Both IL-6 and MCP-1 were significantly higher in AMN astrocytes ($p < 0.01$) compared to CTL and cALD (Fig. 5G). IL-6 levels in cALD astrocytes were significantly lower than CTL ($p < 0.05$); TNF-α and IL-1β were undetectable in culture supernatants of astrocytes (data not shown). We assessed intracellular nitric oxide in CTL, AMN and cALD astrocytes. Basal level of nitric oxide metabolite was higher ($p < 0.05$) in AMN compared to CTL and highest in cALD astrocytes compared to both the CTL and AMN ($p < 0.05$) (Fig 5H).

cALD Astrocytes have Increased STAT3 (Serine^{727}) Phosphorylation and Elevated Toll-Like Receptor Expression

To identify cellular signaling responsible for differential inflammatory responses, we used human phosphor-kinase array proteome profiler. In our proteome profiler, STAT3 phosphorylation at Serine^{727} was shown to be significantly activated in cALD astrocytes (Fig 6A), which was confirmed in densitometry analysis ($p < 0.001$) (Fig 6B) normalized to reference spots in the kinase array and in our immunoblot results (Fig 6C). We also identified hyperphosphorylation of protein kinase (Akt) proteins, mitogen-activated protein kinase (MAPK) p38, stress-activated protein kinases/Jun amino-terminal kinases, and Ras-dependent extracellular signal-regulated kinase (ERK) 1/2 and reduced phosphorylation of β-catenin and adenosine monophosphate-activated protein kinase α1 (AMPKα1) in cALD astrocytes in immunoblot analysis (Fig 6D and E). We also interrogated these astrocytes for Toll-like receptor (TLR) expression. AMN astrocytes showed higher TLR-1, TLR-3 and TLR-5 (all $p < 0.05$) expression compared

bioRxiv preprint doi: https://doi.org/10.1101/2022.09.09.507263; this version posted September 10, 2022. The copyright holder for this preprint (which was not certified by peer review) is the author/funder. All rights reserved. No reuse allowed without permission.

to CTL astrocytes (Fig 6F). TLR-4 levels were significantly decreased ($p < 0.05$) in AMN compared to CTL astrocytes (Fig. 6G). Interestingly cALD astrocytes had increased TLR-1 ($p < 0.001$), TLR-2 ($p < 0.05$), TLR-5 ($p < 0.01$), TLR-6 ($p < 0.05$), TLR-7 ($p < 0.05$), TLR-8 ($p < 0.05$), TLR-9 ($p < 0.05$), and TLR-10 ($p < 0.01$) expression compared to AMN astrocytes. We also observed significantly elevated ($p < 0.05$) expression of Myeloid differentiation factor 88 (MyD88), the major adaptor of TLRs, in cALD astrocytes (Fig. 6G). Furthermore, we observed significant upregulation of NF-κB subunits p52 (NF-κB2) and p65 (RelA) gene expression in cALD astrocytes compared to AMN astrocytes ($p < 0.05$) (Fig 6G).

miRNA-Seq and Analysis of Differentially Expressed miRNA

miRNAs are post-transcriptional regulators of gene expression and act predominantly by silencing their target mRNAs. We examined differential miRNA expression in X-ALD astrocytes through miRNA-Seq. We identified 12 miRNAs (Wald test, False Discovery Rate < 0.05) differentially expressed which classified AMN and cALD from CTL astrocytes. CTL, AMN, and cALD astrocytes are well differentiated by partial least squared discriminant analysis using the first two components (Fig 7A). The 12 differential miRNAs were plotted in box plots (Fig 7B). Hsa-miR-100-5p, hsa-miR-10a-3p, hsa-miR-10a -5p, hsa-miR-335-3p, hsa-miR-339-5p, hsa-miR-409-3p, hsa-miR-9-5p, and hsa-miR-92b-3p were upregulated in AMN astrocytes compared to control astrocytes. On the other hand, hsa-miR-145-3p, hsa-miR-145-5p, and hsa-miR-199b-3p showed lower expression in AMN astrocytes when compared to CTL astrocytes. While hsa-miR-10a-3p, hsa-miR-10a-5p, and hsa-miR-409-3p showed lower expression in cALD astrocytes compared to AMN astrocytes, they showed higher expression when compared to CTL astrocytes. Notable miRNAs were hsa-miR-9-3p and has-miR-9-5p that showed highest expression in cALD astrocytes compared to both AMN and CTL astrocytes. IPA generates networks of interrelated miRNA and other molecules based on their knowledgebase. The top pathway, including 10 of the differential miRNAs, shows how several of the changed metabolites are potentially associated with immune function regulated through IGF1R, IL-17A, and mTOR (Fig 7C). Of note, miR-409-3p is associated with IL-17A, a relationship previously shown in IL-17 stimulated astrocytes releasing inflammatory cytokines and chemokines.[21] In these data, miR-409-3p is increased in AMN and ALD compared to CTL, though the

bioRxiv preprint doi: https://doi.org/10.1101/2022.09.09.507263; this version posted September 10, 2022. The copyright holder for this preprint (which was not certified by peer review) is the author/funder. All rights reserved. No reuse allowed without permission.

levels are lower in cALD than AMN. The other significant pathway was constructed from three of the 12 differential miRNA. The directionality of change in these three miRNAs predicts consistent up and down regulation (orange and blue lines, respectively) of several genes. (Fig 7D).

DISCUSSION

To date, mechanistic underpinnings of differential AMN and cALD phenotypes in X-ALD remain poorly understood. While others have used X-ALD human fibroblasts derived iPSCs to differentiate into brain glial cells,[22, 23] we report comprehensive analyses and novel differences in basal metabolic, biochemical, and inflammatory profile of cALD versus AMN astrocytes. Consistent with previous reports, deleterious ABCD1 variants in patient-fibroblasts did not impede reprogramming and differentiation into astrocytes in our study.[22, 24] Our iPSC-derived astrocytes not only show characteristic X-ALD features including ABCD1 loss and higher VLCFA levels in AMN and cALD compared to CTL but also displayed differential cellular and molecular mechanisms. Heightened STAT3, TLR, and p38 pathways and miR-9 expression in cALD astrocytes may play role in neuroinflammation and a higher expression of CCL2/MCP-1 and IL-6 in AMN astrocytes may be involved in the protective and anti-inflammatory effect. Accumulation of VLCFA causes oxidative stress, affects glycolysis and OXPHOS system,[25] and mitochondrial dysfunction.[4-6] cALD astrocytes demonstrated increased glycolysis, glycolytic capacity, and elevated glycolytic gene expression compared to AMN and CTL. Hyperglycolysis in cALD astrocytes displays a higher energy demand likely making them prone to inflammation compared to AMN astrocytes. While a hyperglycolytic state is implicated in neuroinflammation,[26] activated STAT3 may result in altered mitochondrial energetics.[27] STAT3, a potent inducer of astrogliosis and astrocyte differentiation,[28] can be either activated by the Janus family of kinases or intrinsic tyrosine kinase activity of growth factors and cytokines[29] phosphorylating both serine^{727} and tyrosine^{705}.[30] cALD astrocytes showed activated STAT3-p-serine^{727} and STAT3-p-tyrosine^{705} indicating that cALD astrocytes are highly reactive and activated. Furthermore, elevated neurotrophic factors such as ciliary neurotrophic factor in cALD may also signal through STAT3 and trigger reactive astrocytosis.[31]

bioRxiv preprint doi: https://doi.org/10.1101/2022.09.09.507263; this version posted September 10, 2022. The copyright holder for this preprint (which was not certified by peer review) is the author/funder. All rights reserved. No reuse allowed without permission.

Our analysis revealed a higher DRP-1 expression in cALD than in AMN suggesting higher mitochondrial fission. In line with this, we observed a significant decrease in mtDNA/nuclear DNA ratio in AMN and most decrease in cALD astrocytes suggesting a decrease in mitochondrial content compared to that in CTL astrocytes. Accumulation of dysfunctional mitochondria may result in ROS production. Although, we did not detect increased ROS, cALD astrocytes showed higher expression of superoxide catalyzing NADPH oxidases and overexpression of NDUFA6 in OXPHOS immunoblotting. We observed reduced SDHB (complex II) protein in both AMN and cALD astrocytes compared to CTL astrocytes in OXPHOS immunoblotting implying an impaired electron transport. These data suggest that activated STAT3 may play a role in inflammation in cALD astrocytes and alters mitochondrial-OCR.

mtDNA released by damaged mitochondria due to activated STAT3[27] may further induce endogenous TLR signaling, especially TLR9 signaling. *In vitro*, TLR9 antagonism modulated astrocyte-chemokine release and macrophage chemotaxis in spinal cord injury.[32] In line with this, we also observed higher expression of TLR1-2, and TLR5-10, MyD88 and NF-κB proteins in cALD astrocytes compared to AMN astrocytes. This is also consistent with findings in a X-ALD mouse model spinal cord where upregulated TLR-MyD88-NF-κB pathway was reported.[3, 33] Furthermore, upregulated Akt and p-Akt in cALD astrocytes implies that TLR in association with p-Akt signaling may further trigger reactive astrocytes in cALD patients.[34] Despite lower relative mitochondrial content and higher DRP-1 expression in AMN compared to CTL, AMN astrocytes had lower STAT3 (serine[727]) expression, lower NOX expression, and downregulated TLR expression which potentially underlie the milder non-inflammatory phenotype in AMN.

Increased NAD/NADH ratio is associated with disrupted energy homeostasis. We observed significantly higher intracellular NAD/NADH ratio in both AMN and cALD astrocytes. A previous study reported reduced NAD/NADH ratio in Abcd1-silenced human U87 cells.[35] This discordance may be due to the nature of the source of the U87 cells which is derived from human glioma patient whereas our study used AMN and cALD patient-iPSC-derived astrocytes cultured in basal conditions. Moreover, higher NAD/NADH ratio observed in AMN and cALD astrocytes is likely due to higher glycolysis where NADH

bioRxiv preprint doi: https://doi.org/10.1101/2022.09.09.507263; this version posted September 10, 2022. The copyright holder for this preprint (which was not certified by peer review) is the author/funder. All rights reserved. No reuse allowed without permission.

is oxidized to NAD^+, however, not all NAD^+ is reduced to NADH in mitochondria leading to elevated oxidative metabolic state thus making cells prone to oxidative stress.

We previously documented loss of AMPKα1 in cALD fibroblasts and cALD postmortem brain white matter.[4, 5] AMPKα1 is the master regulator of energy homeostasis and its perturbation is associated with neuroinflammatory diseases.[36] Induction of glycolysis is promoted by growth factors via signal transduction mediated by Akt pathway[37] whereas AMPKα1 is the inhibitor of metabolic switch from OXPHOS to aerobic glycolysis. Consequently, a higher p-Akt and loss of AMPKα1 in cALD astrocytes can explain well the hyper-glycolytic state of astrocytes in cALD compared to AMN and CTL astrocytes.

Th17-linked cytokine IL-17 contributes to inflammation and induces reactive astrocytes and upregulates GFAP and NOS2.[38] We observed an increase in GFAP and AQP4 in AMN and cALD astrocytes along with higher IL-17A, NOS2, TNF-α and interferon-γ in cALD astrocytes suggesting that IL-17 can be a prominent and important mediator of proinflammatory (A1-astrocytes) response in cALD astrocytes.

To identify upstream regulators of inflammatory pathways, we performed comprehensive miRNA profiling by miRNA-Seq in these astrocytes. To the best of our knowledge, this is the first miRNA-Seq study in X-ALD iPSC-derived astrocytes. We observed differentially expressed miRNAs previously not identified in AMN and cALD astrocytes. Most interestingly, we observed a disease-severity associated increase in miR-9-3p and miR-9-5p expression (CTL<AMN<cALD). miR-9-3p is expressed in response to TLRs[39] and upregulation in activated astrocytes mediates microglial migration and activation via phosphatase and tensin (PTEN) homolog.[40] This may result in recruitment of activated microglia in cALD patients. miR-9-5p plays a role in immune regulation and has been reported to contribute to immunity.[41] miR-100-5p serves as extracellular signaling molecule for TLR7/8 and along with miR-298-5p contribute to neurodegeneration in mouse model[42]; however, its role in X-ALD is yet to be explored. miR-10a-3p and miR-10a-5p regulate BDNF expression[43] and we also observed miR-10-3p and miR-10a-5p higher in AMN and cALD astrocytes which may result in lower BDNF expression in these astrocytes. miR-145 is widely known as tumor suppressor miRNA[44] and its overexpression has been shown to be protective in ischemic stroke model of mouse.[45] Based on our IPA analysis, we speculate that miR-145-5p may exert its

bioRxiv preprint doi: https://doi.org/10.1101/2022.09.09.507263; this version posted September 10, 2022. The copyright holder for this preprint (which was not certified by peer review) is the author/funder. All rights reserved. No reuse allowed without permission.

effect on astrocyte proliferation and astrogliosis via interaction with insulin-like growth factor-1 (IGF1R) gene which is crucial for cell growth and proliferation.[46] Additionally, we document upregulated miR-409-3p in AMN and cALD astrocytes compared to CTL astrocytes. The IPA network illustrates that miR-409-3p targets IL-17A and is regulated by IL-17A creating a feedback loop. IL-17A also regulates vascular endothelial growth factor (VEGF) and is in turn regulated by mTOR pathway. Reports exist where miR-409-3p contributes to IL-17-induced inflammatory cytokine production in astrocytes via STAT3 signaling pathway in experimental autoimmune encephalomyelitis (EAE) mice.[21] Interestingly, we recently documented decreased miR-409-3p expression in plasma of AMN patients with increasing disease severity.[47] Similarly, our differential gene IPA network shows that miR-145-3p is associated with HAND1, ATRX, and RAP2C genes. Altered ATRX and RAP2C have been reported to be associated with occurrence of gliomas.[48, 49] However, further studies are needed to explore association of miR-145-3p and these genes in neuroinflammation in AMN and cALD astrocytes.

In AMN astrocytes, in addition to higher expression of immunoregulatory IL-12α, an upregulated IL-6 mRNA expression as well as higher secreted IL-6 cytokine in supernatant was observed compared to control and cALD astrocytes. Although, elevated IL-6 levels have been implicated in neurodegeneration[50] via IL-6 trans-signaling mechanism, based on our findings in the present study, we hypothesize that oncostatin-M upregulation along with TNFα may regulate IL-6 production and higher IL-1RA may mediate anti-inflammatory protective effect in AMN. Moreover, higher levels of chemotactic CCL2 chemokine in AMN astrocytes) and increased CXCL1, 2, 8 and 10 expressions in AMN may play a beneficial role by inducing recruitment of protective and scavenging microglia to the site of inflammation unlike in cALD patient astrocytes.

In conclusion, cALD astrocytes show increased TLR, MyD88 and NF-κB-expression which may mediate activation of STAT3 resulting in mitochondrial stress. Our hypothesis is that, despite possessing monogenic mutation, differential inflammatory responses in severe cALD and milder AMN phenotypes occur involve divergent signaling pathways: A constitutive TLR overactivation disrupts immune homeostasis and MyD88- NF-κB-TLR mediated activated STAT3 leads to neuroinflammatory and

bioRxiv preprint doi: https://doi.org/10.1101/2022.09.09.507263; this version posted September 10, 2022. The copyright holder for this preprint (which was not certified by peer review) is the author/funder. All rights reserved. No reuse allowed without permission.

demyelinating ALD severity. Contrary to this, increased IL-6 expression and elevated MCP-1 secretion by AMN astrocytes may lead to microglial recruitment thus playing key role in chronic inflammation in AMN and inducing protective effects (Fig 8). We believe that our unprecedented findings demonstrate that AMN and cALD patient iPSC-derived astrocytes can mimic inflammatory, biochemical, and molecular variations of cALD and AMN phenotypes associated with common ABCD1 mutation in of X-ALD. Further, we reckon that iPSC-derived astrocytes provide a robust X-ALD model system to study cALD and AMN-specific disease mechanisms. Owing to their pluripotency potential, this system allows us to establish a high-throughput screening system to strategize and identify therapies for cALD and AMN phenotypes of X-ALD.

ACKNOWLEDGMENTS

The authors recognize the Henry Ford Pathology Surgical Electron Microscopy especially Amy Kemper and Cytogenetics Laboratory especially Dr. Brandon Shaw and Samantha Turpen for their contribution to transmission electron microscopy and karyotyping projects, respectively. We also highly acknowledge Stephanie Stebens, at Sladen Library, Henry Ford Hospital for her immense help with the formatting of manuscript for submission to the journal.

AUTHOR CONTRIBUTIONS

JS conceived the idea, designed the experiments, provided direction and funding (NINDS grants R21NS114775 and R01NS114245) for the study. PP, NK, LMP designed and performed the experiments, contributed to the acquisition and analyses of data. PP contributed to drafting the text and preparing the figures with the help from LMP who helped with miRNA data analysis. All authors revised and approved the final version of the manuscript.

CONFLICT OF INTEREST

The authors declare that they have no competing interests to disclose.

bioRxiv preprint doi: https://doi.org/10.1101/2022.09.09.507263; this version posted September 10, 2022. The copyright holder for this preprint (which was not certified by peer review) is the author/funder. All rights reserved. No reuse allowed without permission.

FUNDING

This project was supported by National Institutes of Health (NINDS grants R21NS114775 and R01NS114245 to JS). Funding for this project assisted in the ability to collect and analyze our data.

REFERENCES

1. Moser HW. Adrenoleukodystrophy. Curr Opin Neurol. 1995 Jun;8(3):221-6.

2. Kemp S, Pujol A, Waterham HR, et al. ABCD1 mutations and the X-linked adrenoleukodystrophy mutation database: role in diagnosis and clinical correlations. Human mutation. 2001;18(6):499-515.

3. Singh J, Khan M, Singh I. Silencing of Abcd1 and Abcd2 genes sensitizes astrocytes for inflammation: Implication for X-adrenoleukodystrophy. Journal of Lipid Research. 2009.

4. Singh J, Giri S. Loss of AMP-activated protein kinase in X-linked adrenoleukodystrophy patient-derived fibroblasts and lymphocytes. Biochemical and Biophysical Research Communications. 2014.

5. Singh J, Olle B, Suhail H, Felicella MM, Giri S. Metformin-induced mitochondrial function and ABCD2 up-regulation in X-linked adrenoleukodystrophy involves AMP-activated protein kinase. Journal of Neurochemistry. 2016.

6. Singh J, Suhail H, Giri S. Loss of AMP-activated protein kinase induces mitochondrial dysfunction and proinflammatory response in unstimulated Abcd1-knockout mice mixed glial cells. Mediators of Inflammation. 2015.

7. Lu JF, Lawler AM, Watkins PA, et al. A mouse model for X-linked adrenoleukodystrophy. Proceedings of the National Academy of Sciences of the United States of America. 1997;94(17):9366-71.

bioRxiv preprint doi: https://doi.org/10.1101/2022.09.09.507263; this version posted September 10, 2022. The copyright holder for this preprint (which was not certified by peer review) is the author/funder. All rights reserved. No reuse allowed without permission.

8. Forss-Petter S, Werner H, Berger J, et al. Targeted inactivation of the X-linked adrenoleukodystrophy gene in mice. Journal of neuroscience research. 1997;50(5):829-43.

9. Marchetto MC, Brennand KJ, Boyer LF, Gage FH. Induced pluripotent stem cells (iPSCs) and neurological disease modeling: progress and promises. Human molecular genetics. 2011;20(R2):R109-15.

10. Park I-H, Zhao R, West JA, et al. Reprogramming of human somatic cells to pluripotency with defined factors. Nature. 2008;451(7175):141-6.

11. Mikhail FM, Heerema NA, Rao KW, Burnside RD, Cherry AM, Cooley LD. Section E6.1-6.4 of the ACMG technical standards and guidelines: chromosome studies of neoplastic blood and bone marrow-acquired chromosomal abnormalities. Genet Med. 2016 Jun;18(6):635-42.

12. Zhang Y, Qin Y, Chopp M, et al. Ischemic Cerebral Endothelial Cell-Derived Exosomes Promote Axonal Growth. Stroke. 2020 Dec;51(12):3701-12.

13. Venegas V, Wang J, Dimmock D, Wong LJ. Real-time quantitative PCR analysis of mitochondrial DNA content. Curr Protoc Hum Genet. 2011 Jan;68(1):19.7.1-2.

14. MARTIN M. Cutadapt removes adapter sequences from high-throughput sequencing reads. EMBnet journal. 2011;17.1:10-2.

15. Langmead B, Salzberg SL. Fast gapped-read alignment with Bowtie 2. Nat Methods. 2012 Mar 4;9(4):357-9.

16. Friedlander MR, Mackowiak SD, Li N, Chen W, Rajewsky N. miRDeep2 accurately identifies known and hundreds of novel microRNA genes in seven animal clades. Nucleic Acids Res. 2012 Jan;40(1):37-52.

bioRxiv preprint doi: https://doi.org/10.1101/2022.09.09.507263; this version posted September 10, 2022. The copyright holder for this preprint (which was not certified by peer review) is the author/funder. All rights reserved. No reuse allowed without permission.

17. Love MI, Huber W, Anders S. Moderated estimation of fold change and dispersion for RNA-seq data with DESeq2. Genome Biol. 2014;15(12):550.

18. Pierre Monget JC, FangZou Yao Benoit Liquet. mixOmics: Omics Data Integration Project. R package version 6.1.1. 2016.

19. Paintlia AS GA, Khan M, Singh AK, Barbosa E, Singh I. Correlation of very long chain fatty acid accumulation and inflammatory disease progression in childhood X-ALD: implications for potential therapies. Neurobiol Dis. 2003;14(3):425-39.

20. Weinhofer I, Zierfuss B, Hametner S, et al. Impaired plasticity of macrophages in X-linked adrenoleukodystrophy. Brain. 2018 Aug 1;141(8):2329-42.

21. Liu X, Zhou F, Yang Y, et al. MiR-409-3p and MiR-1896 co-operatively participate in IL-17-induced inflammatory cytokine production in astrocytes and pathogenesis of EAE mice via targeting SOCS3/STAT3 signaling. Glia. 2019 Jan;67(1):101-12.

22. Jang J, Kang HC, Kim HS, et al. Induced pluripotent stem cell models from X-linked adrenoleukodystrophy patients. Ann Neurol. 2011 Sep;70(3):402-9.

23. Baarine M, Khan M, Singh A, Singh I. Functional Characterization of IPSC-Derived Brain Cells as a Model for X-Linked Adrenoleukodystrophy. PLoS One. 2015;10(11):e0143238.

24. Wang XM, Yik WY, Zhang P, et al. The gene expression profiles of induced pluripotent stem cells from individuals with childhood cerebral adrenoleukodystrophy are consistent with proposed mechanisms of pathogenesis. Stem Cell Res Ther. 2012 Oct 4;3(5):39.

25. Fourcade S, Lopez-Erauskin J, Galino J, et al. Early oxidative damage underlying neurodegeneration in X-adrenoleukodystrophy. Hum Mol Genet. 2008 Jun 15;17(12):1762-73.

26. Pamies D SC, Schvartz D, González-Ruiz V, Pellerin L, Nunes C, Tavel D, Maillard V, Boccard J, Rudaz S, Sanchez JC, Zurich MG. . Neuroinflammatory Response to TNFα and IL1β

bioRxiv preprint doi: https://doi.org/10.1101/2022.09.09.507263; this version posted September 10, 2022. The copyright holder for this preprint (which was not certified by peer review) is the author/funder. All rights reserved. No reuse allowed without permission.

Cytokines Is Accompanied by an Increase in Glycolysis in Human Astrocytes In Vitro. Int J Mol Sci. 2021;22(8):4065.

27. Wegrzyn J, Potla R, Chwae Y-J, et al. Function of mitochondrial Stat3 in cellular respiration. Science (New York, NY). 2009;323(5915):793-7.

28. Hong S, Song M-R. STAT3 but not STAT1 is required for astrocyte differentiation. PLoS One. 2014;9(1):e86851-e.

29. Shao H, Cheng HY, Cook RG, Tweardy DJ. Identification and characterization of signal transducer and activator of transcription 3 recruitment sites within the epidermal growth factor receptor. Cancer Res. 2003 Jul 15;63(14):3923-30.

30. Wen Z, Zhong Z, Darnell JE, Jr. Maximal activation of transcription by Stat1 and Stat3 requires both tyrosine and serine phosphorylation. Cell. 1995 Jul 28;82(2):241-50.

31. Herrmann JE IT, Song B, Qi J, Ao Y, Nguyen TK, Korsak RA, Takeda K, Akira S, Sofroniew MV. . STAT3 is a Critical Regulator of Astrogliosis and Scar Formation after Spinal Cord Injury. J Neurosci. 2008;28(28).

32. Li L, Ni L, Heary RF, Elkabes S. Astroglial TLR9 antagonism promotes chemotaxis and alternative activation of macrophages via modulation of astrocyte-derived signals: implications for spinal cord injury. J Neuroinflammation. 2020 Feb 25;17(1):73.

33. Schluter A, Espinosa L, Fourcade S, et al. Functional genomic analysis unravels a metabolic-inflammatory interplay in adrenoleukodystrophy. Hum Mol Genet. 2012 Mar 1;21(5):1062-77.

34. Cheng YY, Ding YX, Bian GL, et al. Reactive Astrocytes Display Pro-inflammatory Adaptability with Modulation of Notch-PI3K-AKT Signaling Pathway Under Inflammatory Stimulation. Neuroscience. 2020 Aug 1;440:130-45.

bioRxiv preprint doi: https://doi.org/10.1101/2022.09.09.507263; this version posted September 10, 2022. The copyright holder for this preprint (which was not certified by peer review) is the author/funder. All rights reserved. No reuse allowed without permission.

35. Baarine M BC, Singh A, Singh I. ABCD1 deletion-induced mitochondrial dysfunction is corrected by SAHA: implication for adrenoleukodystrophy. J Neurochem. 2015;133(3):380-96.

36. Nath N, Khan M, Rattan R, et al. Loss of AMPK exacerbates experimental autoimmune encephalomyelitis disease severity. Biochem Biophys Res Commun. 2009 Aug 14;386(1):16-20.

37. Fox CJ, Hammerman PS, Thompson CB. Fuel feeds function: energy metabolism and the T-cell response. Nat Rev Immunol. 2005 Nov;5(11):844-52.

38. You T, Bi Y, Li J, et al. IL-17 induces reactive astrocytes and up-regulation of vascular endothelial growth factor (VEGF) through JAK/STAT signaling. Sci Rep. 2017 Mar 10;7(1):41779.

39. Bazzoni F, Rossato M, Fabbri M, et al. Induction and regulatory function of miR-9 in human monocytes and neutrophils exposed to proinflammatory signals. Proc Natl Acad Sci U S A. 2009 Mar 31;106(13):5282-7.

40. Yang L, Niu F, Yao H, et al. Exosomal miR-9 Released from HIV Tat Stimulated Astrocytes Mediates Microglial Migration. J Neuroimmune Pharmacol. 2018 Sep;13(3):330-44.

41. Su H, Liang Z, Weng S, et al. miR-9-5p regulates immunometabolic and epigenetic pathways in beta-glucan-trained immunity via IDH3alpha. JCI Insight. 2022 Mar 22;7(6).

42. Wallach T, Mossmann, Z.J., Szczepek, M. et al. MicroRNA-100-5p and microRNA-298-5p released from apoptotic cortical neurons are endogenous Toll-like receptor 7/8 ligands that contribute to neurodegeneration. . Mol Neurodegeneration 2021;80.

43. Zhang T, Liu C, Chi L. Suppression of miR-10a-5p in bone marrow mesenchymal stem cells enhances the therapeutic effect on spinal cord injury via BDNF. Neurosci Lett. 2020 Jan 1;714:134562.

bioRxiv preprint doi: https://doi.org/10.1101/2022.09.09.507263; this version posted September 10, 2022. The copyright holder for this preprint (which was not certified by peer review) is the author/funder. All rights reserved. No reuse allowed without permission.

44. Yoshino H, Enokida H, Itesako T, et al. Tumor-suppressive microRNA-143/145 cluster targets hexokinase-2 in renal cell carcinoma. Cancer Sci. 2013 Dec;104(12):1567-74.

45. Zheng L, Cheng W, Wang X, Yang Z, Zhou X, Pan C. Overexpression of MicroRNA-145 Ameliorates Astrocyte Injury by Targeting Aquaporin 4 in Cerebral Ischemic Stroke. Biomed Res Int. 2017;2017:9530951.

46. Su J, Liang H, Yao W, et al. MiR-143 and MiR-145 regulate IGF1R to suppress cell proliferation in colorectal cancer. PLoS One. 2014;9(12):e114420.

47. Turk BR PL, Nemeth CL, Goodman J, Moser A, Jones RO, Fatemi A, Singh J. MicroRNA and Metabolomics Signatures for Adrenomyeloneuropathy Disease Severity. The Journal of Inherited Metabolic Disease (JIMD) 2022:1-11.

48. Alghamri MS, McClellan BL, Hartlage CS, et al. Targeting Neuroinflammation in Brain Cancer: Uncovering Mechanisms, Pharmacological Targets, and Neuropharmaceutical Developments. Front Pharmacol. 2021;12:680021.

49. Wang X WC, Xi L, Yu Z. Rap2c as a Novel Biomarker for Predicting Poor Prognosis in Glioma. Onco Targets Ther. 2020(13):3073-83.

50. Campbell IL, Abraham CR, Masliah E, et al. Neurologic disease induced in transgenic mice by cerebral overexpression of interleukin 6. Proc Natl Acad Sci U S A. 1993 Nov 1;90(21):10061-5.

bioRxiv preprint doi: https://doi.org/10.1101/2022.09.09.507263; this version posted September 10, 2022. The copyright holder for this preprint (which was not certified by peer review) is the author/funder. All rights reserved. No reuse allowed without permission.

Table 1. List of primer sequences used for RT-qPCR and Antibodies used for Immunoblotting

Target Gene	Forward Primer	Reverse Primer
GFAP	CTGGAGAGGAAGATTGAGTCGC	ACGTCAAGCTCCACATGGACCT
S100-β	GAAGAAATCCGAACTGAAGGAGC	TCCTGGAAGTCACATTCGCCGT
AQP4	GCCATCATTGGAGCAGGAATCC	ACTCAACCAGGAGACCATGACC
ALDH1	CGGGAAAAGCAATCTGAAGAGGG	GATGCGGCTATACAACACTGGC
Nestin	TCAAGATGTCCCTCAGCCTGGA	AAGCTGAGGGAAGTCTTGGAGC
ELOVL1	GTCTACAACTTCTCACTGGTGGC	AAGTGCCTCAGGGCTGTTGGAA
ELOVL3	CTACCTGGTTCTCATCGCTGTG	GTAGCACAGTCCCCATAATGCC
NDUFA6	GACGGGATAAAGTCCGAGAAATG	CATGTGTCCGCTGCTTCCATAC
SDHB	GCAGTCCATAGAAGAGCGTGAG	TGTCTCCGTTCCACCAGTAGCT
SDHC	GGTTCAAACCGTCCTCTGTCTC	CGACATGCCAAAAAGAGAGACCC
UQCRB	TAAGAGGGCACTGGACCTGAAC	CATGATTACTTCTTTGCCCATTCTT
UQCRQ	GCCTATCCGCACGTCTTCACTA	GGATCTCTCGAACTCTTCAGTCC
COX4i-1	TCGGTTTCACCGCGCTCGTTAT	TGTCCAGCATCCTCTTGGTCTG
ATP5B	TCATGCTGAGGCTCCAGAGTTC	ACAGTCTTGCCAACTCCAGCAC
Citrate synthase	CACAGGGTATCAGCCGAACCAA	CCAATACCGCTGCCTTCTCTGT
NRF-1	GGCAACAGTAGCCACATTGGCT	GTCGTCTGGATGGTCATCTCAC
PGC1-α	CCAAAGGATGCGCTCTCGTTCA	CGGTGTCTGTAGTGGCTTGACT
GLUT-1	TTGCAGGCTTCTCCAACTGGAC	CAGAACCAGGAGCACAGTGAAG
HK-I	CTGCTGGTGAAAATCCGTAGTGG	GTCCAAGAAGTCAGAGATGCAGG
HK-II	GAGTTTGACCTGGATGTGGTTGC	CCTCCATGTAGCAGGCATTGCT
GPI	CTGGTAGACGGCAAGGATGTGA	TCCGTGATGGTCTTGCCTGTGT
ALDOC	CATTCTGGCTGCGGATGAGTCT	CACACGGTCATCAGCACTGAAC
GAPDH	GTCTCCTCTGACTTCAACAGCG	ACCACCCTGTTGCTGTAGCCAA

bioRxiv preprint doi: https://doi.org/10.1101/2022.09.09.507263; this version posted September 10, 2022. The copyright holder for this preprint (which was not certified by peer review) is the author/funder. All rights reserved. No reuse allowed without permission.

ENO-1	AGTCAACCAGATTGGCTCCGTG	CACAACCAGGTCAGCGATGAAG
PKM2	ATGGCTGACACATTCCTGGAGC	CCTTCAACGTCTCCACTGATCG
LDHA	GGATCTCCAACATGGCAGCCTT	AGACGGCTTTCTCCCTCTTGCT
NOX1	GGTTTTACCGCTCCCAGCAGAA	CTTCCATGCTGAAGCCACGCTT
NOX2	CTCTGAACTTGGAGACAGGCAAA	CACAGCGTGATGACAACTCCAG
NOX3	CCTGGAAACACGGATGAGTGAG	CCTCCCATAGAAGGTCTTCTGC
NOX4	GCCAGAGTATCACTACCTCCAC	CTCGGAGGTAAGCCAAGAGTGT
IFN-γ	GAGTGTGGAGACCATCAAGGAAG	TGCTTTGCGTTGGACATTCAAGTC
IL-12α	TGCCTTCACCACTCCCAAAACC	CAATCTCTTCAGAAGTGCAAGGG
IL-12β	GACATTCTGCGTTCAGGTCCAG	CATTTTTGCGGCAGATGACCGTG
IL-1β	CCACAGACCTTCCAGGAGAATG	GTGCAGTTCAGTGATCGTACAGG
IL-6	AGACAGCCACTCACCTCTTCAG	TTCTGCCAGTGCCTCTTTGCTG
NOS-2	GCTCTACACCTCCAATGTGACC	CTGCCGAGATTTGAGCCTCATG
IL-23α	GAGCCTTCTCTGCTCCCTGATA	GACTGAGGCTTGGAATCTGCTG
IL-1R	GTGCTTTGGTACAGGGATTCCTG	CACAGTCAGAGGTAGACCCTTC
IL-1RA	ATGGAGGGAAGATGTGCCTGTC	GTCCTGCTTTCTGTTCTCGCTC
TNF-α	CTCTTCTGCCTGCTGCACTTTG	ATGGGCTACAGGCTTGTCACTC
IL-17A	CGGACTGTGATGGTCAACCTGA	GCACTTTGCCTCCCAGATCACA
IL-22	GTTCCAGCCTTATATGCAGGAGG	GCACATTCCTCTGGATATGCAGG
ARG-1	TCATCTGGGTGGATGCTCACAC	GAGAATCCTGGCACATCGGGAA
FIZZ-1	GCAAGAAGCTCTCGTGTGCTAG	AACATCCCACGAACCACAGCCA
IL-4	CCGTAACAGACATCTTTGCTGCC	GAGTGTCCTTCTCATGGTGGCT
IL-10	TCTCCGAGATGCCTTCAGCAGA	TCAGACAAGGCTTGGCAACCCA
MRC-1	AGCCAACACCAGCTCCTCAAGA	CAAAACGCTCGCGCATTGTCCA
CCL-2	AGAATCACCAGCAGCAAGTGTCC	TCCTGAACCCACTTCTGCTTGG

bioRxiv preprint doi: https://doi.org/10.1101/2022.09.09.507263; this version posted September 10, 2022. The copyright holder for this preprint (which was not certified by peer review) is the author/funder. All rights reserved. No reuse allowed without permission.

CCL-3	ACTTTGAGACGAGCAGCCAGTG	TTTCTGGACCCACTCCTCACTG
CCL-4	GCTTCCTCGCAACTTTGTGGTAG	GGTCATACACGTACTCCTGGAC
CCL-5	CCTGCTGCTTTGCCTACATTGC	ACACACTTGGCGGTTCTTTCGG
CCL-22	TCCTGGGTTCAAGCGATTCTCC	GTCAGGAGTTCAAGACCAGCCT
CCR-1	CAACTCCGTGCCAGAAGGTGAA	GTTCAGGAGGTAGATGCTGGTC
CCR-2	CAGGTGACAGAGACTCTTGGGA	GGCAATCCTACAGCCAAGAGCT
CCR-3	TACTCCCTGGTGTTCACTGTGG	ACGAGGAAGAGCAGGTCCGAAA
CCR-5	TCTCTTCTGGGCTCCCTACAAC	CCAAGAGTCTCTGTCACCTGCA
CCR-8	TGGCTGTTGTCCATGCCGTGTA	TGGGATGGTAGCCATAATGGCG
CXCL1	AGCTTGCCTCAATCCTGCATCC	TCCTTCAGGAACAGCCACCAGT
CXCL2	GGCAGAAAGCTTGTCTCAACCC	CTCCTTCAGGAACAGCCACCAA
CXCL8	GAGAGTGATTGAGAGTGGACCAC	CACAACCCTCTGCACCCAGTTT
CXCL10	GGTGAGAAGAGATGTCTGAATCC	GTCCATCCTTGGAAGCACTGCA
CXCL12	CTCAACACTCCAAACTGTGCCC	CTCCAGGTACTCCTGAATCCAC
BDNF	CATCCGAGGACAAGGTGGCTTG	GCCGAACTTTCTGGTCCTCATC
CNTF	TCAGACCTGACTGCTCTTACGG	TTGGAGTCGCTCTGCCTCGGT
GDNF	CGCCGAAGACCGCTCCCTCG	ATCCATGACATCATCGAACTGATC
NGF	ACCCGCAACATTACTGTGGACC	GACCTCGAAGTCCAGATCCTGA
NTF3	CAAGCAGATGGTGGACGTTAAGG	TCGCAGCAGTTCGGTGTCCATT
NTF4/5	GCAAGGCTGATAACGCTGAGGA	CCTGGGCATCAGCGGTCAATG
TLR-1	CAGCGATGTGTTCGGTTTTCCG	GATGGGCAAAGCATGTGGACCA
TLR-2	CTTCACTCAGGAGCAGCAAGCA	ACACCAGTGCTGTCCTGTGACA
TLR-3	GCGCTAAAAAGTGAAGAACTGGAT	GCTGGACATTGTTCAGAAAGAGG
TLR-4	CCCTGAGGCATTTAGGCAGCTA	AGGTAGAGAGGTGGCTTAGGCT
TLR-5	CCTTACAGCGAACCTCATCCAC	TCCACTACAGGAGGAGAAGCGA

bioRxiv preprint doi: https://doi.org/10.1101/2022.09.09.507263; this version posted September 10, 2022. The copyright holder for this preprint (which was not certified by peer review) is the author/funder. All rights reserved. No reuse allowed without permission.

TLR-6	ACTGACCTTCCTGGATGTGGCA	TGACCTCATCTTCTGGCAGCTC
TLR-7	CTTTGGACCTCAGCCACAACCA	CGCAACTGGAAGGCATCTTGTAG
TLR-8	ACTCCAGCAGTTTCCTCGTCTC	AAAGCCAGAGGGTAGGTGGGAA
TLR-9	TGAGCCACAACTGCATCTCGCA	CAGTCGTGGTAGCTCCGTGAAT
TLR-10	GGTTAAAAGACGTTCATCTCCACG	CCTAGCATCCTGAGATACCAGG
mtDNA tRNA Leu (UUR) gene	CACCCAAGAACAGGGTTTGT	TGGCCATGGGTATGTTGTTA
nuclear gene β2-microglobulin	TGCTGTCTCCATGTTTGATGTATCT	TCTCTGCTCCCCACCTCTAAGT

Antigen	Clone	Isotype	Supplier	Cat. No.	Dilution
ABCD1	EPR15929	Rabbit IgG	Abcam	ab197013	1:1000
ABCD2	Polyclonal	Rabbit IgG	Abcam	ab97383	1:1000
ABCD3	EPR5614	Rabbit IgG	Abcam	ab109448	1:1000
Oxphos	Ms mAb cocktail	Cocktail	Abcam	ab110413	6 ug/ml
GFAP	Polyclonal	Rabbit IgG	Abcam	ab7260	1:10000
p-Akt	D9E	Rabbit IgG	CST	4060S	1:1000
Total Akt	C67E7	Rabbit IgG	CST	4692S	1:1000
p-AMPK	40H9	Rabbit IgG	CST	2535L	1:1000
Total-AMPK	Polyclonal	Rabbit IgG	CST	2757S	1:1000
p-P44	D13.14.4E	Rabbit IgG	CST	4370S	1:1000
Total-p44	137F5	Rabbit IgG	CST	4695S	1:1000
p-SAP/JNK	81E11	Rabbit IgG	CST	4668S	1:1000
Total-SAP/JNK	Polyclonal	Rabbit IgG	CST	9252	1:1000

bioRxiv preprint doi: https://doi.org/10.1101/2022.09.09.507263; this version posted September 10, 2022. The copyright holder for this preprint (which was not certified by peer review) is the author/funder. All rights reserved. No reuse allowed without permission.

P-Stat sampler kit	Sampler kit	Rabbit IgG	CST	9914T	1:1000
Total-stat3	79D7	Rabbit IgG	CST	4904S	1:1000
S100-beta	E7C3A	Rabbit IgG	CST	90393S	1:1000
EAAT1	D20D5	Rabbit IgG	CST	5685S	1:1000
AQP4	D1F8E	Rabbit IgG	CST	59678S	1:1000
ALDH1L1	E7I2Q	Rabbit IgG	CST	85828S	1:1000
Glut-1	D3J3A	Rabbit IgG	CST	12939S	1:1000
Hexokinase-I	C35C4	Rabbit IgG	CST	2024S	1:1000
Hexokinase-II	C64G5	Rabbit IgG	CST	2867S	1:1000
DRP-1	C-5	Mouse IgG1	SantaCruz Biotechnology	Sc-271583	1:500
Mitofusin-1	D6E2S	Rabbit IgG	CST	14739	1:1000
PKM2	D78A4	Rabbit IgG	CST	4053S	1:1000
PGC1α	3G6	Rabbit IgG	CST	2178S	1:1000
iNOS	E3W6B	Rabbit IgG	CST	20609S	1:1000
Beta-actin	D6A8	Rabbit IgG	CST	8457S	1:2000
HRP-anti-rabbit		Goat anti-rabbit IgG	CST	7074S	1:2000
HRP-anti-mouse		Horse anti-mouse IgG	CST	7076S	1:2000

bioRxiv preprint doi: https://doi.org/10.1101/2022.09.09.507263; this version posted September 10, 2022. The copyright holder for this preprint (which was not certified by peer review) is the author/funder. All rights reserved. No reuse allowed without permission.

FIGURE LEGENDS

Figure 1: X-ALD fibroblasts can be successfully reprogrammed into iPSCs and thence differentiated into patient astrocytes. (A) Representative phase contrast (upper panel) and immunostained images of CTL, AMN, and cALD iPSCs. Upper panel shows morphology in culture (day 3) of reprogrammed CTL, AMN, and cALD iPSCs. Middle and lower panel represent phase contrast images for immunostaining for pluripotency markers: CTL, AMN, and cALD iPSCs with positive staining of OCT4 (green), SOX2 (red), NANOG (green), and TRA1-60 (red) (scale bars 150 µm). Nuclei are stained with DAPI (blue). (B) Phase contrast images (upper panel) of differentiated CTL, AMN, and cALD astrocytes in culture (day 1) and immunofluorescence staining (lower panels) with astrocyte specific markers: CTL, AMN, and cALD astrocytes stained positive with GFAP/Nestin (green/red), AQP4/Tuj1 (green/red), S100-β/ALDH1 (green/red), and EAAT1/A2B5 (green/red) (scale bars 150 µm). Nuclei are stained with DAPI (blue). (C) Representative images for Western blotting with GFAP, S100-β, EAAT1, AQP4, ALDH1, and β-actin in CTL, AMN, and cALD astrocytes. (D) RT-qPCR quantification of gene expression for GFAP, S100-β, AQP4, ALDH1, and Nestin for CTL, AMN, and cALD astrocytes (n = 3 technical replicates per line for astrocytes). The gene expression of the individual sample was assessed with fold change using the comparative $\Delta\Delta Ct$ method by normalizing with reference gene L-27 in CTL, AMN, and cALD astrocytes. Results represent means ± standard error from triplicates of each sample type. Two-tailed Student's *t* test was used for data presented in 1D. Significance was assigned denoted for P values of less than 0.05. $^{*}P < 0.05$, $^{**}P < 0.01$; $^{***}P < 0.001$. (E-G) Karyotype analysis for CTL (E), AMN (F), and cALD (G) astrocytes. **Abbreviations**: AMN: Adrenomyeloneuropathy; cALD: Cerebral adrenoleukodystrophy; CTL: Control; iPSC: Induced pluripotent stem cells.

Figure 2: CTL, AMN, and cALD patient astrocytes retain biochemical characteristics of X-ALD patients. (A) Representative images for Western blotting with ABCD1, ABCD2, and ABCD3, and β-actin in CTL, AMN, and cALD patient astrocytes. (B) Quantification of VLCFA (ratio C24:0/C22:0 and C24:1/C22:0; C26:0/C22:0 and C26:1/C22:0) in astrocytes generated from CTL, AMN, and cALD astrocytes. (C) RT-qPCR quantification of gene expression for ELOVL1 and ELOVL3 in CTL, AMN, and

bioRxiv preprint doi: https://doi.org/10.1101/2022.09.09.507263; this version posted September 10, 2022. The copyright holder for this preprint (which was not certified by peer review) is the author/funder. All rights reserved. No reuse allowed without permission.

cALD astrocytes (n = 3 technical replicates per line for astrocytes). The gene expression of the individual sample was assessed with fold change using the comparative ΔΔ*Ct* method by normalizing with reference gene L-27 in CTL, AMN, and cALD astrocytes. Results (Figures B and C) represent means ± standard error from triplicates of each of sample type. Two-tailed Student's *t* test was used for data analysis. Significance was assigned for P values of less than 0.05. $^{*}P < 0.05$, $^{**}P < 0.01$; $^{***}P < 0.001$. **Abbreviations**: AMN: Adrenomyeloneuropathy; cALD: Cerebral adrenoleukodystrophy; CTL: Control; VLCFA: Very long chain fatty acids.

Figure 3: cALD astrocytes show altered parameters of OCR and ECAR in cell mito stress and glycolytic stress test assays. (A) Plot showing overall OCR in CTL, AMN, and cALD astrocytes. (B) Quantification of basal and non-mitochondrial OCR. (C) Quantification of proton leak and ATP-linked OCR. (D) Quantification of maximal respiration and spare respiratory capacity. (E) Quantification of mitochondrial ATP production rate (pmol ATP/minute). (F) Plot showing the overall ECAR in CTL, AMN, and cALD astrocytes. (G) Quantification of glycolysis and non-glycolytic acidification. (H) Quantification of glycolytic capacity and glycolytic reserve. (I) Quantification of percent glycolytic reserve. (J) Quantification of glycolytic ATP production rate (pmol ATP/minute).

Data information: Results represent means ± standard error (N = 3 technical replicates) of each of sample type. Analysis was performed using the Wave software (version 2.6.1.53; Agilent) and normalized to the cell protein content (A-D and F-I). Data analysis in figures E and J was performed after acquisition of data using XF Real-Time ATP rate assay generator (Agilent, Santa Clara, CA) (N = 3 technical replicates) for each sample type. Unpaired two-tailed Student's *t* test or Mann-Whitney test were used for analysis. Significance was denoted for P values of less than 0.05. $^{*}P < 0.05$, $^{**}P < 0.01$; $^{***}P < 0.001$. Significance level over AMN bars represent difference between CTL and AMN astrocyte samples and that over cALD bars represent the difference between AMN and cALD astrocyte samples. **Abbreviations**: AMN: Adrenomyeloneuropathy; cALD: Cerebral adrenoleukodystrophy; CTL: Control; ECAR: Extracellular acidification rate; OCR: Oxygen consumption rate; OM: Oligomycin; FCCP: Carbonyl cyanide-4

bioRxiv preprint doi: https://doi.org/10.1101/2022.09.09.507263; this version posted September 10, 2022. The copyright holder for this preprint (which was not certified by peer review) is the author/funder. All rights reserved. No reuse allowed without permission.

(trifluoromethoxy) phenylhydrazone; Rot/AA: Rotenone and antimycin-A; Glu: Glucose; OM: Oligomycin; 2-DG: 2-deoxi-D-glucose.

Figure 4: X-ALD patients show decreased mitochondrial content. Mitochondrial structural and functional assessment using TEM and RT-qPCR. (A) Representative TEM images of CTL, AMN, and cALD astrocytes. Upper panel (A1-A3 at scale bars 2 µm) represent whole CTL, AMN, and cALD astrocyte. Middle (A4-A6) and lower (A7-A9) represent mitochondrial structures in CTL, AMN, and cALD astrocytes (scale bars 1 µm and 400 nm, respectively). N: Nucleus; M: Mitochondria; ER: Endoplasmic reticulum; L: Lipid droplets. (B) Western blotting with DRP-1, mitofusin-1, and β-actin in CTL, AMN, and cALD astrocytes. (C) Quantification of DRP-1 (ratio against β-actin) in CTL, AMN, and cALD astrocytes (n = 3 technical replicates per line for astrocytes run in three independent blots). (D) RT-qPCR quantification of gene expression for mitochondrial genes (NDUFA6, SDHB, SDHC, UQCRB, UQCRQ, Cox4i-1, ATP5B, citrate synthase, and PGC1α) for CTL, AMN, and cALD astrocytes (n = 3 technical replicates per line for astrocytes). (E) Representative images for Western blotting with total OXPHOS at low exposure (bottom blot) and high exposure (top blot) and β-actin in CTL, AMN, and cALD astrocytes. (F) RT-qPCR quantification of gene expression for glycolytic genes (Glut-1, HK-I, HK-II, GPI, ALDOC, GapDH, EN-1, PKM2, and LDHA) for CTL, AMN, and cALD astrocytes (n = 3 technical replicates per line for astrocytes). (G) Representative images for Western blotting with Glut-I, HK-I, HK-II, PKM2, and and β-actin in CTL, AMN, and cALD astrocytes. (H) Quantification of reactive oxygen species (mean fluorescence intensity) between CTL, AMN, and cALD patient groups (n = 3 technical replicates per line for astrocytes). (I) RT-qPCR quantification of gene expression for NOX1, NOX2, NOX3, and NOX4 for CTL, AMN, and cALD astrocytes (n = 3 technical replicates per line for astrocytes). (J) Quantification of mitochondrial DNA to nuclear DNA ratio in CTL, AMN, and cALD astrocytes (n = 3 technical replicates per line for astrocytes). (K) Quantification of NAD/NADH levels in CTL, AMN, and cALD astrocytes (n = 3 technical replicates per line for astrocytes). Color scheme shows colors assigned to sample types in qRT-PCR plots.

bioRxiv preprint doi: https://doi.org/10.1101/2022.09.09.507263; this version posted September 10, 2022. The copyright holder for this preprint (which was not certified by peer review) is the author/funder. All rights reserved. No reuse allowed without permission.

Data Information: Data in C represents corrected mean pixel density (pixel density – background) measured in 3 independent blots of DRP-1 on the samples (n = 3) and calculated as ratio of mean pixel density for DRP-1/β-actin. Data analyses for D, F, I, and J were performed using CFX Maestro software (version 5.3.022.1030; Bio-Rad Laboratories, Hercules, CA) and the values represent mean means ± standard error. The gene expression of the individual sample was assessed with fold change using the comparative ΔΔ*Ct* method by normalizing with reference gene L-27 in CTL, AMN, and cALD astrocytes. The values in J are plotted as mitochondrial/nuclear DNA of AMN and cALD with reference to CTL. The values in K is NAD/NADH ratio measured by reading absorbance at 450 nm using a NAD^+ standard curve. Unpaired two-tailed Student's *t* test or Mann-Whitney test were used for analysis. Significance was denoted for P values of less than 0.05. $^{*}P < 0.05$, $^{**}P < 0.01$; $^{***}P < 0.001$. **Abbreviations**: AMN: Adrenomyeloneuropathy; cALD: Cerebral adrenoleukodystrophy; CTL: Control; DRP-1: Dynamin related protein-1; mtDNA: Mitochondrial DNA; nDNA: Nuclear DNA; TEM: Transmission electron microscopy.

Figure 5: cALD astrocytes reveal an increased proinflammatory cytokine expression and a higher nitrite concentration. (A & B) RT-qPCR quantification of gene expression for proinflammatory (IFN-γ, IL-12α, IL-12β, IL-1β, IL-6, Nos2, IL-23α, IL-1R, IL-RA, TNF-α, IL-17A, and IL-22) (A) and anti-inflammatory (Arg-1, Fizz-1, IL-4, IL-10, and MRC-1) (B) in CTL, AMN, and cALD astrocytes (n = 3 technical replicates per line for astrocytes). The gene expression of the individual sample was assessed with fold change using the comparative ΔΔ*Ct* method by normalizing with reference gene L-27 in CTL, AMN, and cALD astrocytes. (C-E) RT-qPCR quantification of gene expression for C-C motif chemokine ligands (CCL-2, CCL-3, CCL-4, CCL-5, and CCL-22) (C), C-C motif chemokine receptors (CCR-1, CCR-2, CCR-3, CCR-5, and CCR-8) (D), and C-X-C motif chemokine ligands (CXCL1, CXCL2, CXCL8, CXCL10, and CXCL12) (E) in CTL, AMN, and cALD astrocytes (n = 3 technical replicates per line for astrocytes). (F) RT-qPCR quantification of gene expression for neurotrophic factors (BDNF, CNTF, GDNF, NGF, NTF3, and NTF4/5) for CTL, AMN, and cALD astrocytes (n = 3 technical replicates per line for astrocytes). The gene expression of the individual sample was assessed with fold change using the comparative ΔΔ*Ct* method by normalizing with reference gene L-27 in CTL, AMN, and cALD astrocytes. (G) Quantification

bioRxiv preprint doi: https://doi.org/10.1101/2022.09.09.507263; this version posted September 10, 2022. The copyright holder for this preprint (which was not certified by peer review) is the author/funder. All rights reserved. No reuse allowed without permission.

of IL-12p40, IL-6, and MCP-1 in the culture supernatant of CTL, AMN, and cALD astrocytes. Results represent means ± standard error (pg/mL) from triplicates of each sample type (n = 3). (H) Quantification of nitrites in CTL, AMN, and cALD astrocyte lysates. Panel H represents the nitrites (OD and pmoles per µg protein) calculated using standard curve in the panel C. Color scheme shows colors assigned to sample types in qRT-PCR plots.

Data information: Results represent means ± standard error from triplicates of each sample type. Two-tailed Student's *t* test or Mann-Whitney tests were performed to analyze the data. Significance was denoted for P values of less than 0.05. $^{*}P < 0.05$, $^{**}P < 0.01$; $^{***}P < 0.001$. **Abbreviations**: AMN: Adrenomyeloneuropathy; cALD: Cerebral adrenoleukodystrophy; CTL: Control; OD: Optical density (absorbance).

Figure 6: cALD astrocytes show higher Stat3 and TLR activity. (A & B) Phosphokinase antibody array blots using CTL, AMN, and cALD patient astrocyte lysates (250 µg for each of antibody array membranes) (A) and Kinase phosphorylation analysis using mean pixel density showing basal level changes in the expression levels of Stat3, JNK1/2/3, p38 α, SRC, Stat5 A/B, β-catenin, and Akt1/2/3 activity in CTL, AMN, and cALD astrocytes (B). (C) Representative images for Western blotting with p-Stat3 (ser727), p-Stat3 (tyr705), total Stat3, and β-actin in CTL, AMN, and cALD astrocytes. (D & E) Representative images for Western blotting with phosphorylated and total Akt, β-catenin, and p38 (D) and SAP/JNK, Erk1/2, and AMPK (E) in CTL, AMN, and cALD astrocytes. β-actin was used as reference CTL. (F & G) RT-qPCR quantification of gene expression for TLR (TLR1-10) (G) and MyD88, p52 NFκB, and p65 NFκB (H) for CTL, AMN, and cALD astrocytes (n = 3 technical replicates per line for astrocytes). The gene expression of the individual sample was assessed with fold change using the comparative $\Delta\Delta Ct$ method by normalizing with reference gene L-27 in CTL, AMN, and cALD astrocytes. Color scheme shows colors assigned to sample types in qRT-PCR plots.

Data information: Results represent means ± standard error from triplicates of each sample type. Two-tailed Student's *t* test or Mann-Whitney tests were performed to analyze the data. Significance was denoted for P values of less than 0.05. $^{*}P < 0.05$, $^{**}P < 0.01$; $^{***}P < 0.001$. **Abbreviations**: AMN:

bioRxiv preprint doi: https://doi.org/10.1101/2022.09.09.507263; this version posted September 10, 2022. The copyright holder for this preprint (which was not certified by peer review) is the author/funder. All rights reserved. No reuse allowed without permission.

Adrenomyeloneuropathy; cALD: Cerebral adrenoleukodystrophy; CTL: Control; Stat3: Signal transducer and activator of transcription 3; TLR: Toll-like receptor.

Figure 7: CTL, AMN, and cALD patient astrocytes retain biochemical characteristics of X-ALD patients. (A) Partial least squares discriminant analysis (PLSDA) score plots of significant miRNAs determined by miRNA sequence analysis of CTL, AMN, and cALD patient astrocytes (n = 5 technical replicates of each sample type). (B) Box plots of 12 significant miRNAs determined by miRNA sequencing of CTL, AMN, and cALD iPSC-derived astrocytes. (n = 5 technical replicates of each sample type). (C & D) Ingenuity pathway gene network generated by comparing differentially expressed miRNAs and regulatory pathways in CTL, AMN, and cALD astrocytes. **Abbreviations**: AMN: Adrenomyeloneuropathy; cALD: Cerebral adrenoleukodystrophy; CTL: Control; miRNA: microRNA; PLSDA: Partial Least Square-Discriminant Analysis

Figure 8: Summarized schematic of study findings and possible mechanisms in AMN and cALD astrocytes. We believe that our findings for the first time show that X-ALD patient-iPSC derived astrocytes can recapitulate molecular and biochemical functional differences and is a robust system to model AMN and cALD phenotypes of X-ALD. In AMN astrocytes, we observed activated IL-6 that induces Stat3 phosphorylation via gp130-associated JAK/STAT and MAPK and transactivates anti-inflammatory genes especially arginase-1 and mannose receptor C-type-1. Furthermore, higher production of monocyte chemoattractant protein-1 in culture supernatant can be helpful in recruiting protective and scavenging microglia which phagocytose and clear cell debris. On the other hand, cALD patient astrocytes show heightened MyD88-NFκB-TLR activity that fully activate and phosphorylate serine 727 and tyrosine 705-Stat3 resulting in increased proinflammatory cytokines IFN-γ, IL-23α, TNF-α, Nos2, IL-17A, and IL-22. Elevated NOX expression and reduced SDHB and UQCRQ activity in addition to Stat3 activation is detrimental to mitochondria. Substantial increased TLR activity, mitochondrial dysfunction, and simultaneous hyperglycolytic state are potential contributors to neuroinflammation in cALD astrocytes. Our findings support our belief that AMN astrocytes show anti-inflammatory (A2) phenotype whereas cALD astrocytes demonstrate highly reactive and proinflammatory (A1) phenotype. **Abbreviations**: AMN:

bioRxiv preprint doi: https://doi.org/10.1101/2022.09.09.507263; this version posted September 10, 2022. The copyright holder for this preprint (which was not certified by peer review) is the author/funder. All rights reserved. No reuse allowed without permission.

Adrenomyeloneuropathy; Arg-1: Arginase-1; cALD: Cerebral adrenoleukodystrophy; MCP-1: Monocyte chemoattractant protein-1; MRC-1: Mannose receptor c-type-1; SRE: Signaling response elements; TLR: Toll-like receptors.

bioRxiv preprint doi: https://doi.org/10.1101/2022.09.09.507263; this version posted September 10, 2022. The copyright holder for this preprint (which was not certified by peer review) is the author/funder. All rights reserved. No reuse allowed without permission.

FIGURE 1

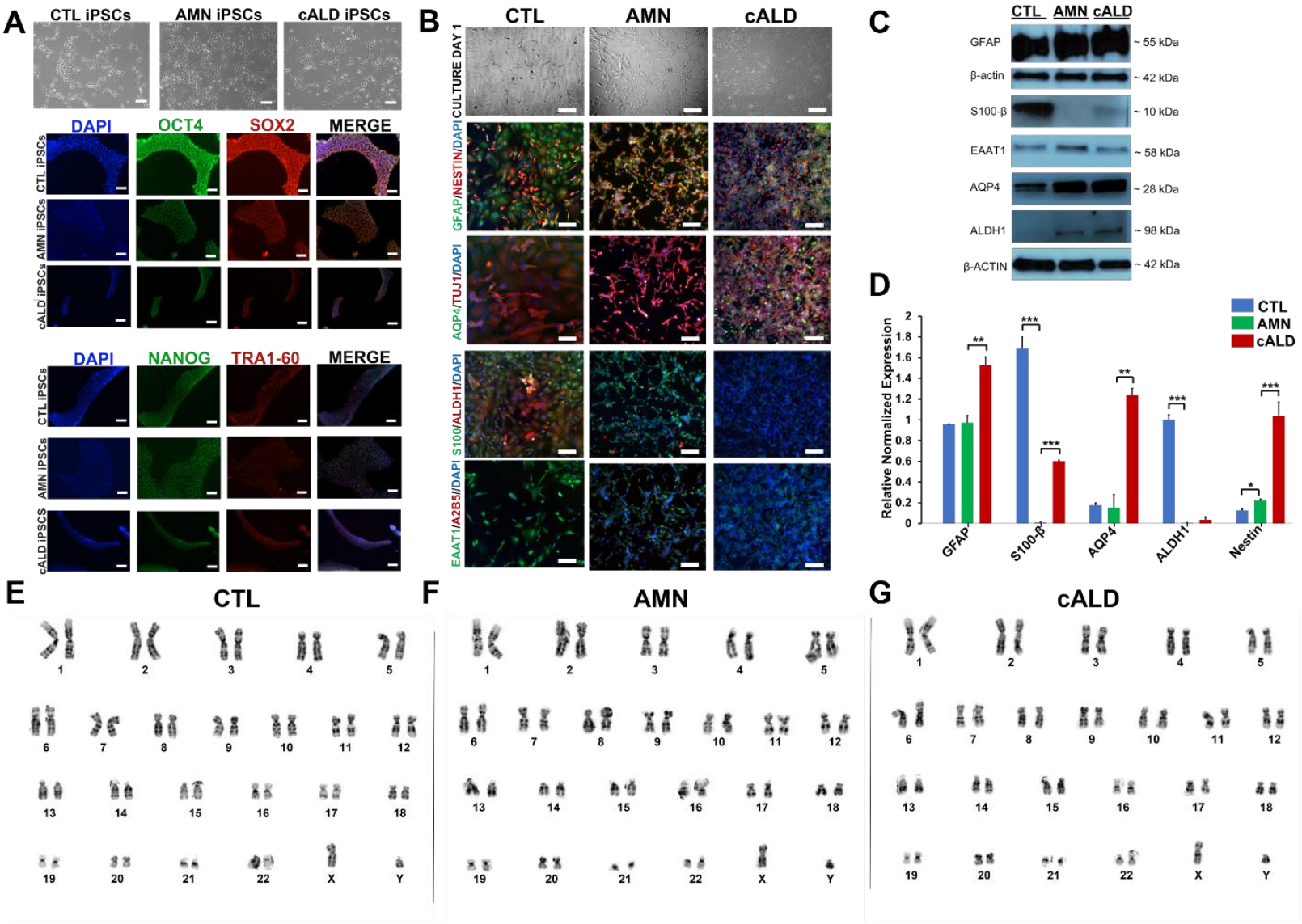

bioRxiv preprint doi: https://doi.org/10.1101/2022.09.09.507263; this version posted September 10, 2022. The copyright holder for this preprint (which was not certified by peer review) is the author/funder. All rights reserved. No reuse allowed without permission.

FIGURE 2

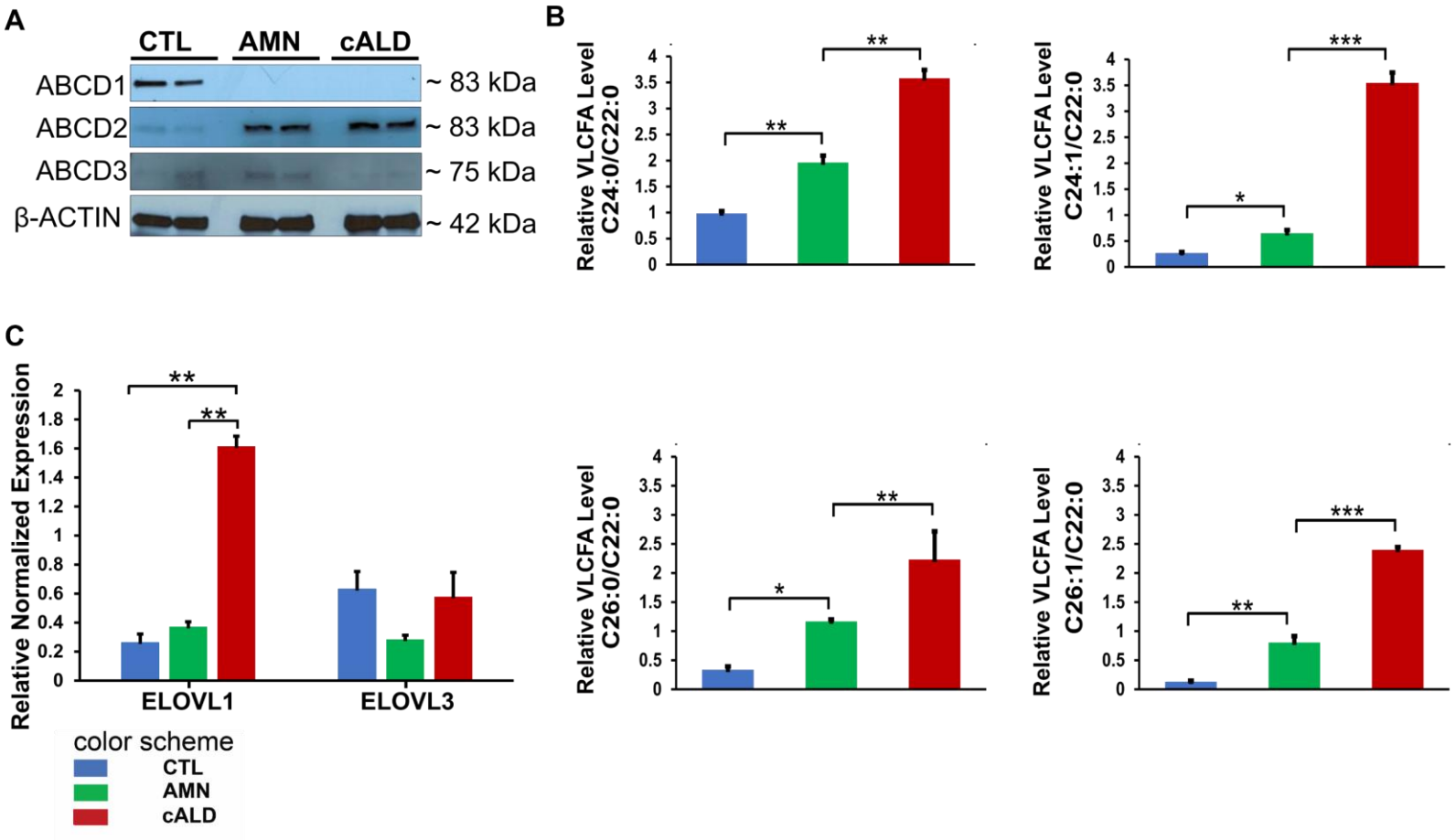

bioRxiv preprint doi: https://doi.org/10.1101/2022.09.09.507263; this version posted September 10, 2022. The copyright holder for this preprint (which was not certified by peer review) is the author/funder. All rights reserved. No reuse allowed without permission.

FIGURE 3

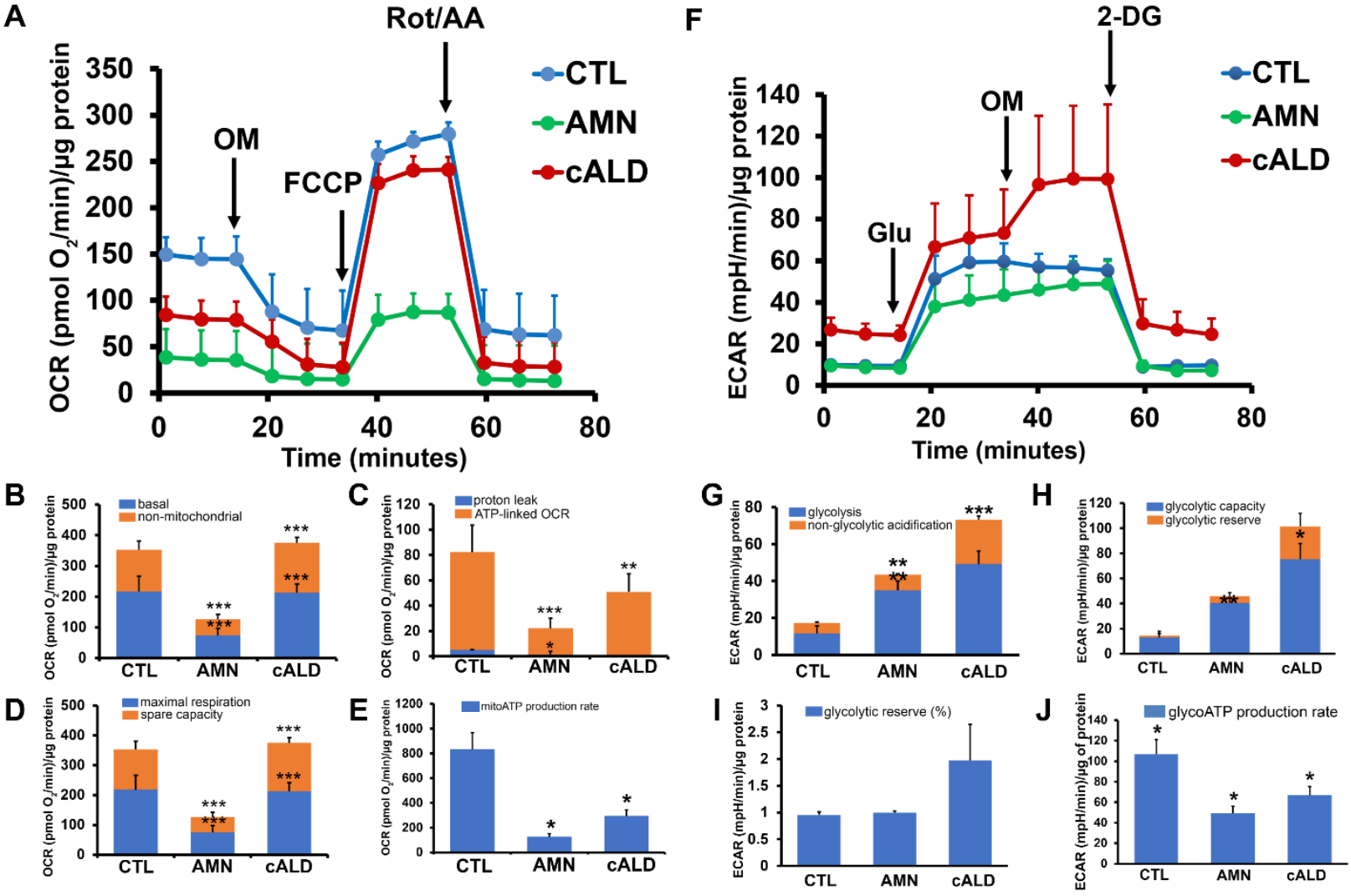

bioRxiv preprint doi: https://doi.org/10.1101/2022.09.09.507263; this version posted September 10, 2022. The copyright holder for this preprint (which was not certified by peer review) is the author/funder. All rights reserved. No reuse allowed without permission.

FIGURE 4

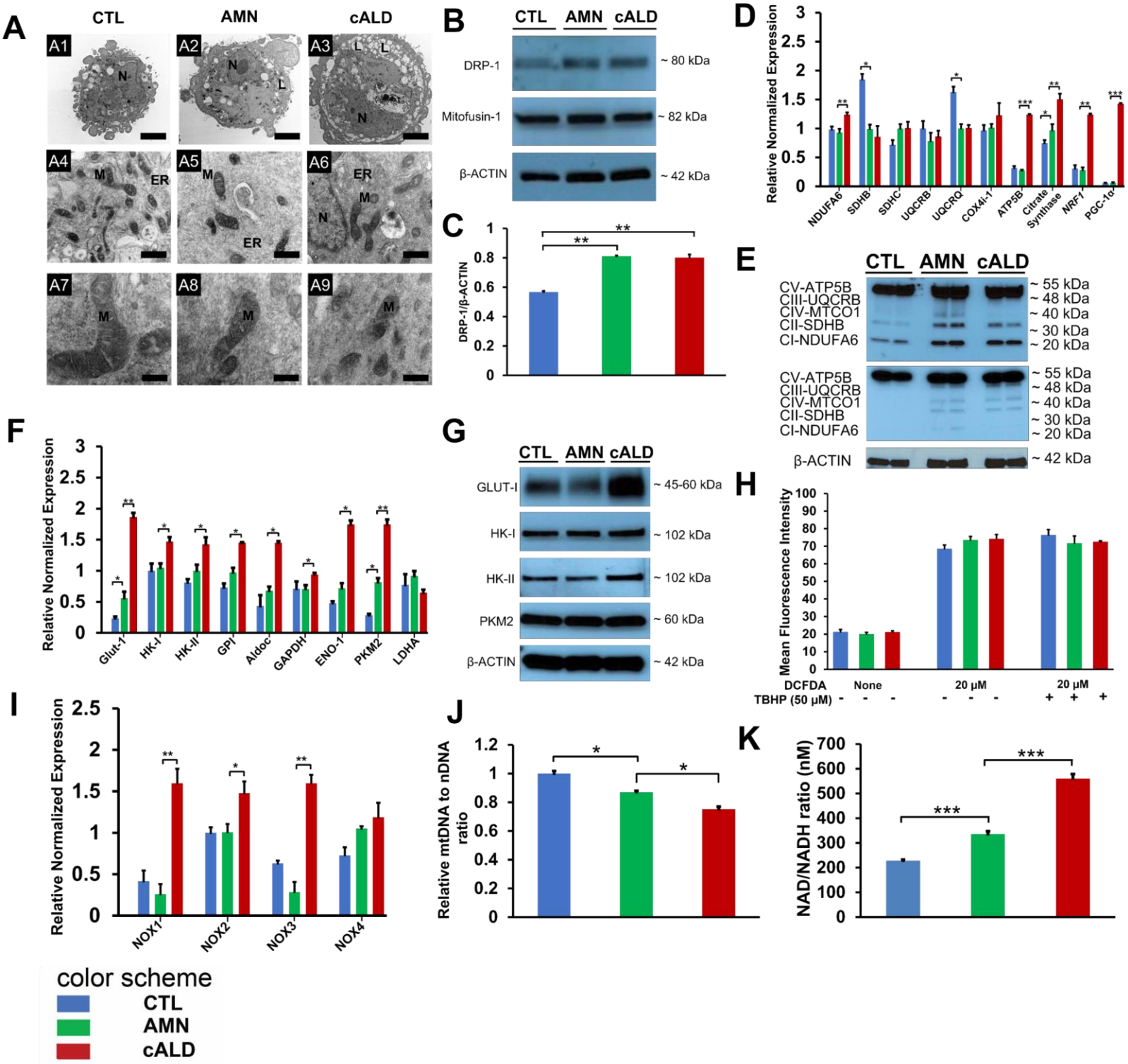

bioRxiv preprint doi: https://doi.org/10.1101/2022.09.09.507263; this version posted September 10, 2022. The copyright holder for this preprint (which was not certified by peer review) is the author/funder. All rights reserved. No reuse allowed without permission.

FIGURE 5

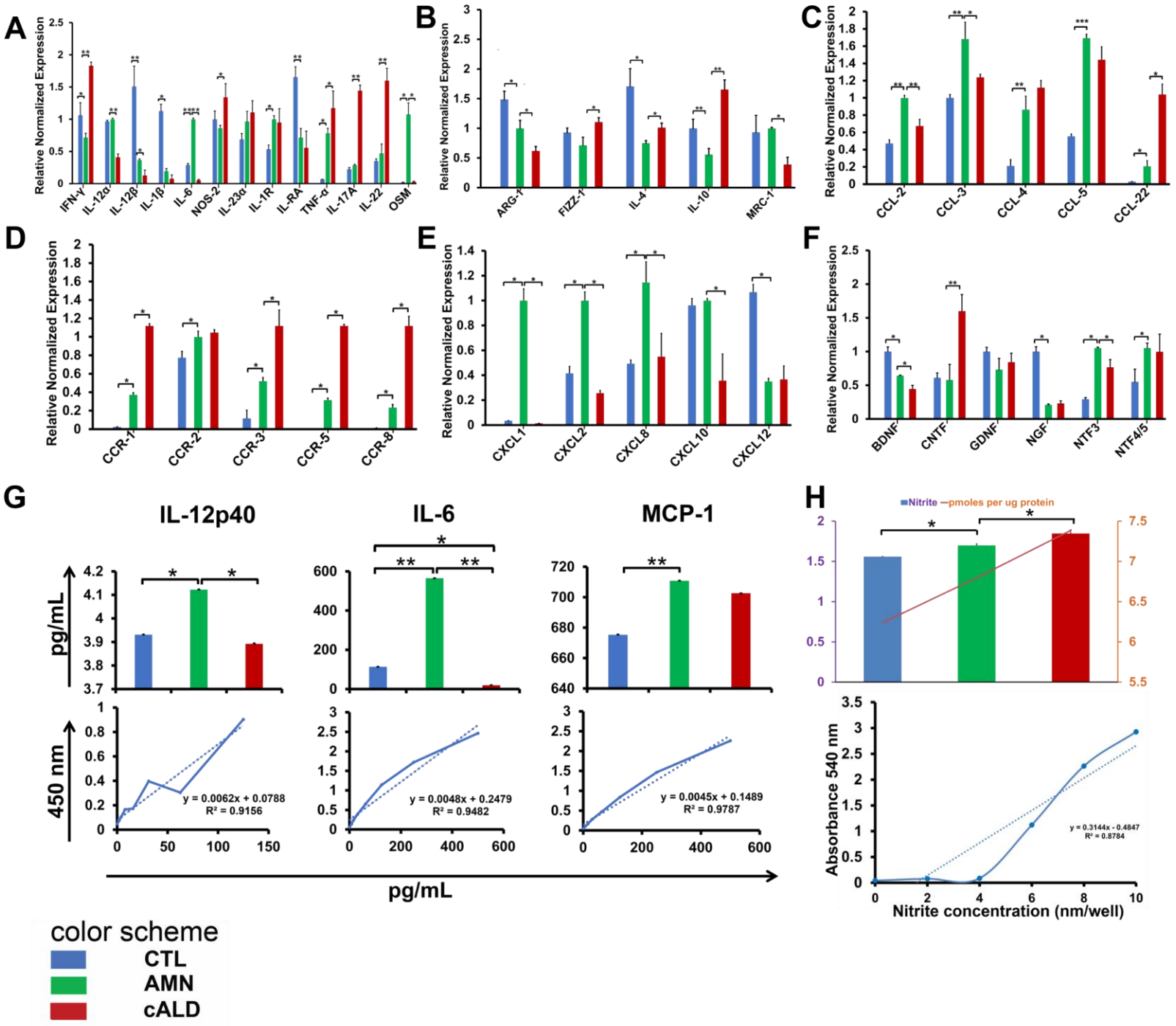

bioRxiv preprint doi: https://doi.org/10.1101/2022.09.09.507263; this version posted September 10, 2022. The copyright holder for this preprint (which was not certified by peer review) is the author/funder. All rights reserved. No reuse allowed without permission.

FIGURE 6

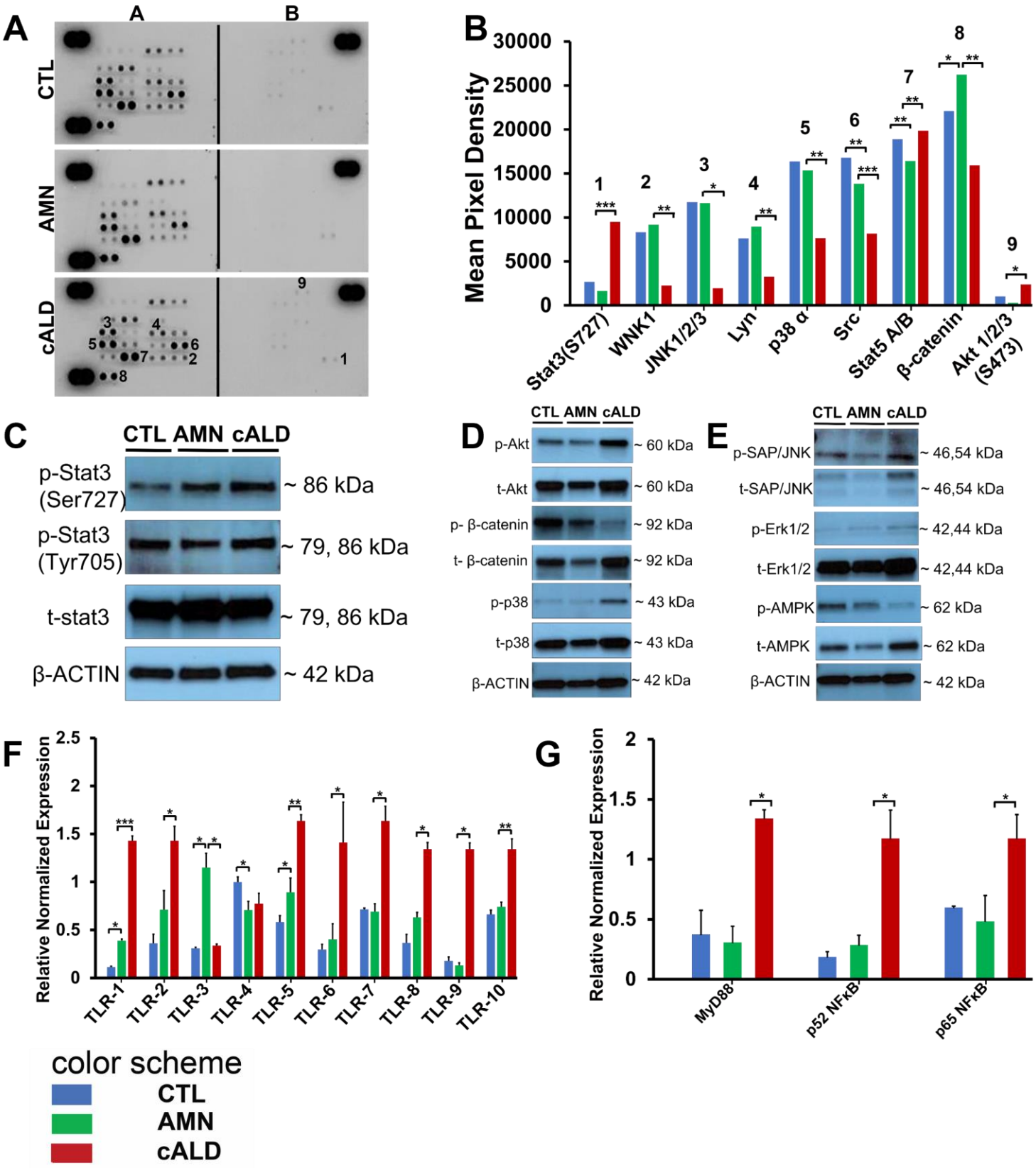

bioRxiv preprint doi: https://doi.org/10.1101/2022.09.09.507263; this version posted September 10, 2022. The copyright holder for this preprint (which was not certified by peer review) is the author/funder. All rights reserved. No reuse allowed without permission.

FIGURE 7

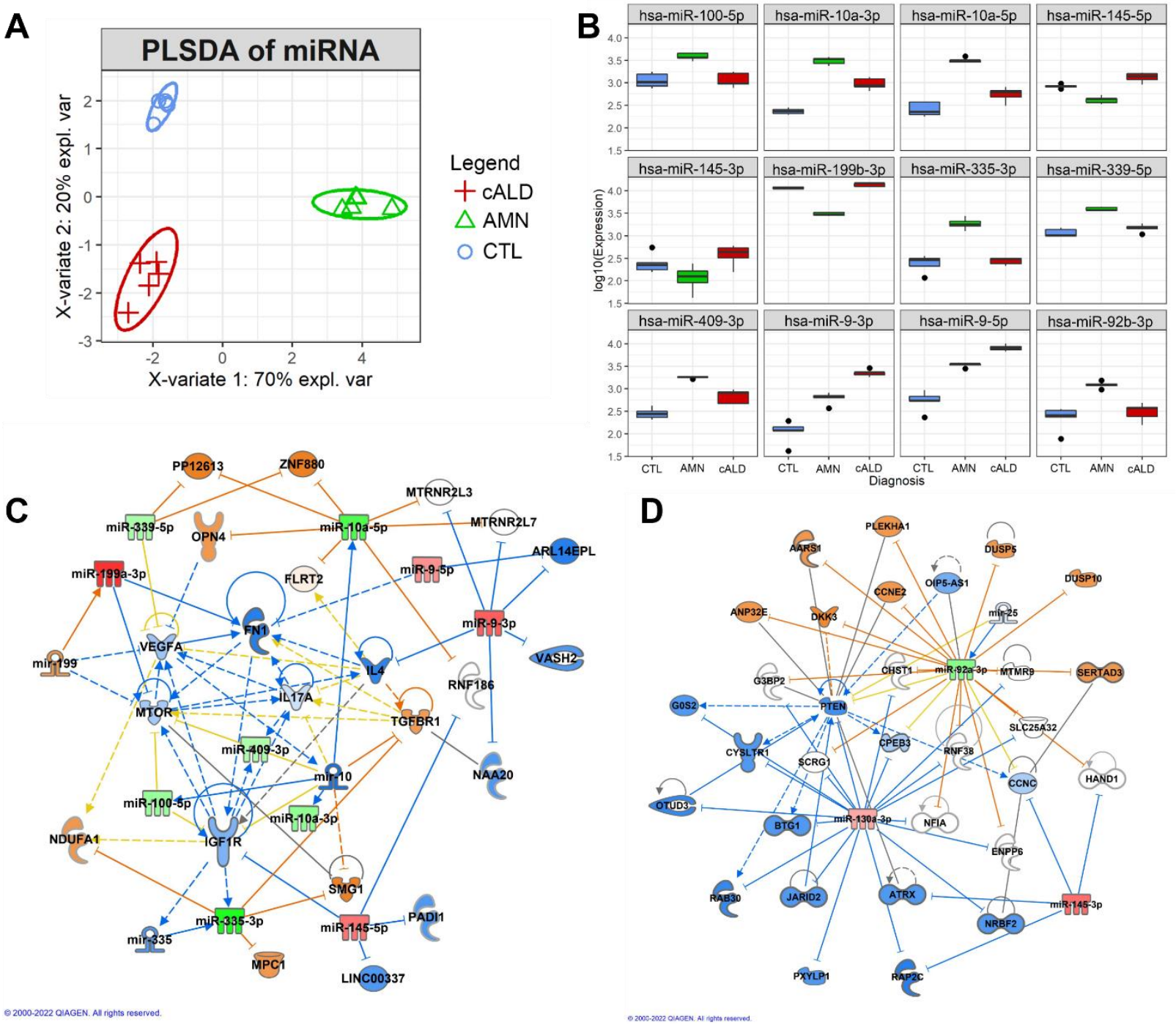

bioRxiv preprint doi: https://doi.org/10.1101/2022.09.09.507263; this version posted September 10, 2022. The copyright holder for this preprint (which was not certified by peer review) is the author/funder. All rights reserved. No reuse allowed without permission.
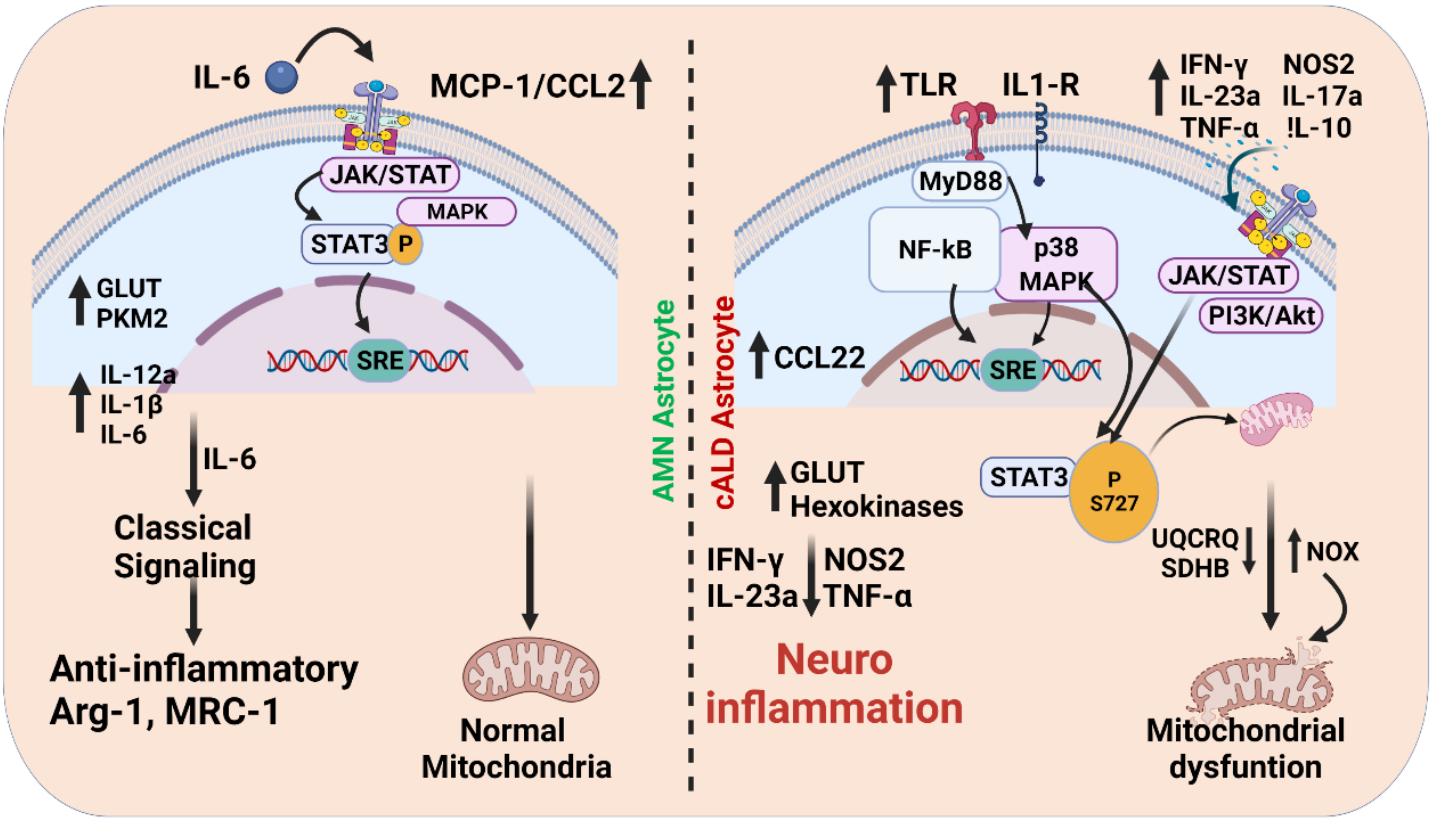
FIGURE 8